Synthesis of Novel Integrated Actuators Powered by Shape Memory Alloys

THIS IS A TEMPORARY TITLE PAGE
It will be replaced for the final print by a version
provided by the registrar's office.

Thèse n. 1234 2021
présentée le 28 juin 2021
à la Faculté des sciences de base
Integrated Actuators Laboratory
Programme Doctoral en Robotics, Control, and Intelligent Systems
École polytechnique fédérale de Lausanne

pour l'obtention du grade de Docteur ès Sciences
par

Sean Thomas

acceptée sur proposition du jury :

Prof Name Surname, président du jury
Prof Name Surname, directeur de thèse
Prof Name Surname, rapporteur
Prof Name Surname, rapporteur
Prof Name Surname, rapporteur

Lausanne, EPFL, 2021

Wings are a constraint that makes
it possible to fly.
— Robert Bringhurst

To my parents. . .

Acknowledgements

Lorem ipsum dolor sit amet, consectetuer adipiscing elit. Ut purus elit, vestibulum ut, placerat ac, adipiscing vitae, felis. Curabitur dictum gravida mauris. Nam arcu libero, nonummy eget, consectetuer id, vulputate a, magna. Donec vehicula augue eu neque. Pellentesque habitant morbi tristique senectus et netus et malesuada fames ac turpis egestas. Mauris ut leo. Cras viverra metus rhoncus sem. Nulla et lectus vestibulum urna fringilla ultrices. Phasellus eu tellus sit amet tortor gravida placerat. Integer sapien est, iaculis in, pretium quis, viverra ac, nunc. Praesent eget sem vel leo ultrices bibendum. Aenean faucibus. Morbi dolor nulla, malesuada eu, pulvinar at, mollis ac, nulla. Curabitur auctor semper nulla. Donec varius orci eget risus. Duis nibh mi, congue eu, accumsan eleifend, sagittis quis, diam. Duis eget orci sit amet orci dignissim rutrum.

Nam dui ligula, fringilla a, euismod sodales, sollicitudin vel, wisi. Morbi auctor lorem non justo. Nam lacus libero, pretium at, lobortis vitae, ultricies et, tellus. Donec aliquet, tortor sed accumsan bibendum, erat ligula aliquet magna, vitae ornare odio metus a mi. Morbi ac orci et nisl hendrerit mollis. Suspendisse ut massa. Cras nec ante. Pellentesque a nulla. Cum sociis natoque penatibus et magnis dis parturient montes, nascetur ridiculus mus. Aliquam tincidunt urna. Nulla ullamcorper vestibulum turpis. Pellentesque cursus luctus mauris.

Lausanne, June 28, 2021 D. K.

Preface

A preface is not mandatory. It would typically be written by some other person (eg your thesis director).

Lorem ipsum dolor sit amet, consectetuer adipiscing elit. Ut purus elit, vestibulum ut, placerat ac, adipiscing vitae, felis. Curabitur dictum gravida mauris. Nam arcu libero, nonummy eget, consectetuer id, vulputate a, magna. Donec vehicula augue eu neque. Pellentesque habitant morbi tristique senectus et netus et malesuada fames ac turpis egestas. Mauris ut leo. Cras viverra metus rhoncus sem. Nulla et lectus vestibulum urna fringilla ultrices. Phasellus eu tellus sit amet tortor gravida placerat. Integer sapien est, iaculis in, pretium quis, viverra ac, nunc. Praesent eget sem vel leo ultrices bibendum. Aenean faucibus. Morbi dolor nulla, malesuada eu, pulvinar at, mollis ac, nulla. Curabitur auctor semper nulla. Donec varius orci eget risus. Duis nibh mi, congue eu, accumsan eleifend, sagittis quis, diam. Duis eget orci sit amet orci dignissim rutrum.

Nam dui ligula, fringilla a, euismod sodales, sollicitudin vel, wisi. Morbi auctor lorem non justo. Nam lacus libero, pretium at, lobortis vitae, ultricies et, tellus. Donec aliquet, tortor sed accumsan bibendum, erat ligula aliquet magna, vitae ornare odio metus a mi. Morbi ac orci et nisl hendrerit mollis. Suspendisse ut massa. Cras nec ante. Pellentesque a nulla. Cum sociis natoque penatibus et magnis dis parturient montes, nascetur ridiculus mus. Aliquam tincidunt urna. Nulla ullamcorper vestibulum turpis. Pellentesque cursus luctus mauris.

Lausanne, 12 Mars 2011 T. D.

Abstract

Lorem ipsum dolor sit amet, consectetuer adipiscing elit. Ut purus elit, vestibulum ut, placerat ac, adipiscing vitae, felis. Curabitur dictum gravida mauris. Nam arcu libero, nonummy eget, consectetuer id, vulputate a, magna. Donec vehicula augue eu neque. Pellentesque habitant morbi tristique senectus et netus et malesuada fames ac turpis egestas. Mauris ut leo. Cras viverra metus rhoncus sem. Nulla et lectus vestibulum urna fringilla ultrices. Phasellus eu tellus sit amet tortor gravida placerat. Integer sapien est, iaculis in, pretium quis, viverra ac, nunc. Praesent eget sem vel leo ultrices bibendum. Aenean faucibus. Morbi dolor nulla, malesuada eu, pulvinar at, mollis ac, nulla. Curabitur auctor semper nulla. Donec varius orci eget risus. Duis nibh mi, congue eu, accumsan eleifend, sagittis quis, diam. Duis eget orci sit amet orci dignissim rutrum.

Nam dui ligula, fringilla a, euismod sodales, sollicitudin vel, wisi. Morbi auctor lorem non justo. Nam lacus libero, pretium at, lobortis vitae, ultricies et, tellus. Donec aliquet, tortor sed accumsan bibendum, erat ligula aliquet magna, vitae ornare odio metus a mi. Morbi ac orci et nisl hendrerit mollis. Suspendisse ut massa. Cras nec ante. Pellentesque a nulla. Cum sociis natoque penatibus et magnis dis parturient montes, nascetur ridiculus mus. Aliquam tincidunt urna. Nulla ullamcorper vestibulum turpis. Pellentesque cursus luctus mauris.

Zusammenfassung

Lorem ipsum dolor sit amet, consectetuer adipiscing elit. Ut purus elit, vestibulum ut, placerat ac, adipiscing vitae, felis. Curabitur dictum gravida mauris. Nam arcu libero, nonummy eget, consectetuer id, vulputate a, magna. Donec vehicula augue eu neque. Pellentesque habitant morbi tristique senectus et netus et malesuada fames ac turpis egestas. Mauris ut leo. Cras viverra metus rhoncus sem. Nulla et lectus vestibulum urna fringilla ultrices. Phasellus eu tellus sit amet tortor gravida placerat. Integer sapien est, iaculis in, pretium quis, viverra ac, nunc. Praesent eget sem vel leo ultrices bibendum. Aenean faucibus. Morbi dolor nulla, malesuada eu, pulvinar at, mollis ac, nulla. Curabitur auctor semper nulla. Donec varius orci eget risus. Duis nibh mi, congue eu, accumsan eleifend, sagittis quis, diam. Duis eget orci sit amet orci dignissim rutrum.

Nam dui ligula, fringilla a, euismod sodales, sollicitudin vel, wisi. Morbi auctor lorem non justo. Nam lacus libero, pretium at, lobortis vitae, ultricies et, tellus. Donec aliquet, tortor sed accumsan bibendum, erat ligula aliquet magna, vitae ornare odio metus a mi. Morbi ac orci et nisl hendrerit mollis. Suspendisse ut massa. Cras nec ante. Pellentesque a nulla. Cum sociis natoque penatibus et magnis dis parturient montes, nascetur ridiculus mus. Aliquam tincidunt urna. Nulla ullamcorper vestibulum turpis. Pellentesque cursus luctus mauris.

Résumé

Lorem ipsum dolor sit amet, consectetuer adipiscing elit. Ut purus elit, vestibulum ut, placerat ac, adipiscing vitae, felis. Curabitur dictum gravida mauris. Nam arcu libero, nonummy eget, consectetuer id, vulputate a, magna. Donec vehicula augue eu neque. Pellentesque habitant morbi tristique senectus et netus et malesuada fames ac turpis egestas. Mauris ut leo. Cras viverra metus rhoncus sem. Nulla et lectus vestibulum urna fringilla ultrices. Phasellus eu tellus sit amet tortor gravida placerat. Integer sapien est, iaculis in, pretium quis, viverra ac, nunc. Praesent eget sem vel leo ultrices bibendum. Aenean faucibus. Morbi dolor nulla, malesuada eu, pulvinar at, mollis ac, nulla. Curabitur auctor semper nulla. Donec varius orci eget risus. Duis nibh mi, congue eu, accumsan eleifend, sagittis quis, diam. Duis eget orci sit amet orci dignissim rutrum.

Nam dui ligula, fringilla a, euismod sodales, sollicitudin vel, wisi. Morbi auctor lorem non justo. Nam lacus libero, pretium at, lobortis vitae, ultricies et, tellus. Donec aliquet, tortor sed accumsan bibendum, erat ligula aliquet magna, vitae ornare odio metus a mi. Morbi ac orci et nisl hendrerit mollis. Suspendisse ut massa. Cras nec ante. Pellentesque a nulla. Cum sociis natoque penatibus et magnis dis parturient montes, nascetur ridiculus mus. Aliquam tincidunt urna. Nulla ullamcorper vestibulum turpis. Pellentesque cursus luctus mauris.

Contents

Introduction

A non-numbered chapter...

Lorem ipsum dolor sit amet, consectetuer adipiscing elit. Ut purus elit, vestibulum ut, placerat ac, adipiscing vitae, felis. Curabitur dictum gravida mauris. Nam arcu libero, nonummy eget, consectetuer id, vulputate a, magna. Donec vehicula augue eu neque. Pellentesque habitant morbi tristique senectus et netus et malesuada fames ac turpis egestas. Mauris ut leo. Cras viverra metus rhoncus sem. Nulla et lectus vestibulum urna fringilla ultrices. Phasellus eu tellus sit amet tortor gravida placerat. Integer sapien est, iaculis in, pretium quis, viverra ac, nunc. Praesent eget sem vel leo ultrices bibendum. Aenean faucibus. Morbi dolor nulla, malesuada eu, pulvinar at, mollis ac, nulla. Curabitur auctor semper nulla. Donec varius orci eget risus. Duis nibh mi, congue eu, accumsan eleifend, sagittis quis, diam. Duis eget orci sit amet orci dignissim rutrum.

1 Overview of SMA Actuator Design

In this chapter, the traditional design methodology of the SMA actuator is presented. Here, the different building blocks and state-of-the-art of various SMA actuators are presented. An in-depth look at the advantages and limitations of the methodology is conducted.

1.1 Introduction

1.2 Traditional SMA Actuator Design

1.3 Building Blocks of SMA Actuator Design

1.4 SMA Powered Robotic Systems

1.5 Summary and Conclusion

2 Predicting the Shape Memory Effect

In this chapter, different modelling strategies, such as finite element modelling and analytical modelling, are presented. Here, the modelling techniques are employed in the context of the traditional SMA actuator design methodology. Furthermore, the bias spring actuator model and a simplified model are presented.

2.1 Introduction

2.2 Analytical Modelling of the SME

2.3 Finite Element Modelling

2.4 Stroke Estimation of SMA Actuators

2.4.1 Mechanical Modelling

2.4.2 Thermal Model

2.5 Simplified SMA Actuator Model

2.6 Summary and Conclusion

3 Sizing Methodology of Biasing Kinematics Stages for SMA Actuators

3.1 Introduction

In the past few decades, there has been a growing need for miniaturisation. Modern devices have come to require actuators that are compact and lightweight. As mentioned previously, since SMAs have been known to show the highest volumetric work density, they have been increasingly used in applications where compactness and low weight are required.

As previously presented in chapter 1, SMA actuators require an active element, a biasing element and a kinematic stage for motion control. These components, usually discrete elements, when combined together create an SMA actuator that can preform a specific reversible work, such as gripping or crawling motionscite. With the objective of miniaturisation, most work has been conducted into rendering these individual components as compact and lightweight as possiblecite. But the fact that these stages are discrete, lowers the overall volumetric work density of the complete actuator. Furthermore, as multiple systems are needed, the actuator also requires various pieces and assembly increasing the complexity and decreasing the compactness.

Recently, there has been a shift in creating novel motion control mechanisms using flexure-based mechanisms. These flexures are multiple compliant elements designed so as to only be compliant in specific degrees of freedom while being rigid in the others. These mechanisms, which can be fabricated using a monolithic piece of material, are lightweight and require virtually no assembly. These flexural stages, when paired with SMAs, have greatly increased the overall work density of the traditional SMA actuatorscite.

These flexure-based mechanisms are still often integrated into the SMA actuators as discrete mechanisms. In this chapter, the concept of integrating the biasing element as a flexural mechanism is explored. In this case, the kinematic stage and the biasing element are combined and are no longer discrete systems within the mechanism. Some research has been shown to take into account flexure mechanisms in SMA actuators but they lack a suitable sizing strategy due to the complexity of the shape memory effect and the nonlinear nature of flexurescite.

Thus, in this chapter, this novel design methodology is presented and analysed using an analytical model.

3.2 Adapted Design Concept

As mentioned previously, most SMA actuators are composed of an active element, a biasing element and a kinematic stage charged with converting the linear output of the actuator into a more complex one. In general, these elements are discrete components ranging from SMA coils, passive biasing springs and the kinematic stage comprised of hinges and linear slides. As presented in fig. 3.1, the design methodology consists of integrating the kinematic stage and the biasing element.

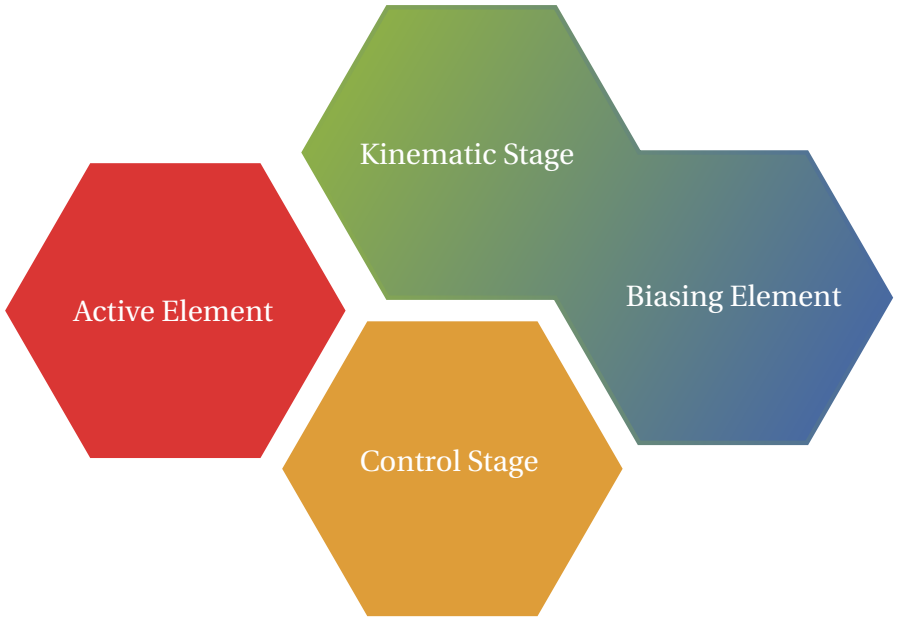

Figure 3.1: Diagram of the adapted building blocks of the SMA actuator.

This integration can be accomplished with the use of flexure-based mechanisms. Generally, flexures have been used in creating an alternative solution for traditional hinges and linear slides. These flexures are comprised of cantilever beams which allows the mechanism to be compliant in a specific degree of freedom while being rigid in the others. The advantages of such a system is that when adequately design can result in a kinematic stage that is lightweight, lacks any assembly and has high precision.

The main drawback to such a system compared to traditional bearings is the inherent stiffness of the mechanism. As these flexures are composed of compliant beams, the rigidity of the beam must be taken into account. In the case of an SMA actuator, this rigidity of the compliant structure can be harnessed as the biasing element. This implies that by pairing the active SMA element with a flexure, the kinematic stage and the biasing element can be combined. This novel approach can be used to create biased SMA actuators that are precise, lightweight and

with a limited number of pieces to be assembled.

3.3 Challenges of the Approach

Due to the complex nature of the shape memory effect, the principle challenge when it comes to designing such SMA actuators is the difficulty in sizing the active SMA based on the flexure mechanism. Based on the configuration of the flexural stage, this mechanism can present highly nonlinear behaviour as well. When paired with an SMA wire or coil, this can results in unintended behaviours or secondary operating points.

Recently there has been research such as the work by Maffiodo et al. (2017) that shows the advantages of pairing SMA wires with flexure-based structures. As with this case, the sizing of the SMA element is disregarding and the biasing advantage of the flexure is neglected.

In the case of grippers and mesoscale actuators where the SMA element is passively cooled, the accurate sizing of the SMA is important. In designs, where passive cooling is used, the geometry of the active element is critical as the shape and structure of the active element is directly related to the cooling times. In the case of SMA coils and wires, thinner diameters imply a shorter cooling time. These thinner wires, however, result in smaller forces when heated. This implies that by accurately sizing the SMA element for the biasing flexure, the actuator can be made as thin as possible while still being able to deform the flexure during heating. Thus, by adapting the traditional sizing methodology of bias-spring SMA actuators for flexure-based designs, the SMA actuator can be designed with faster response times.

3.4 Adapting the Simplified Models

In section 2.5, a simplified model of the SMAs are used to size the active element for bias-spring and antagonistic SMA actuators. In the traditional sizing strategy, a simplified linear model of the SMA and the curve of the spring are used to find the operating points of the actuator which is represented by the intersection of the two curves. This simplification allows a relatively simpler sizing of the components by abstracting the complex nonlinear behaviours of the shape memory effect.

3.4.1 Passive Biasing Compliant Mechanisms

The compliant mechanism, as mentioned previously, acts as the biasing element and as the kinematic stage that produces the desired actuator motion. Here, the basic principle is that the inherent stiffness of the compliant flexure mechanism is harnessed to pre-load the SMA for activation. In this case, at lower temperatures, the SMA is deformed using the energy stored in the compliant mechanism while at higher temperatures, the strain recovered by the shape memory effect is used to deform the compliant mechanism. Based on the design of the

compliant mechanism, the SMA actuator can be made to actuate reversibly in a single degree of freedom while being rigid in the others.

In order to size the actuator and its corresponding passive biasing compliant element, an analytical model can be devised and exploited to predict the various operating points of the final SMA actuator. A pseudo-rigid body model (PSBM) based on the work by Henein (2005) can be used to devise the analytical models of the flexures. The flexure hinges are considered to behave like torsional springs with constant angular stiffness, K_θ. The analytical model can be derived by considering the reaction force exerted by the mechanism on the SMA wire or coil when acting as the biasing element.

While a Newtonian approach is possible, the simplest way to compute the force is to consider the elastic potential energy stored in the flexure hinges as the mechanism deforms. This potential energy stored in one torsional spring as a function of the input displacement of the mechanism, x, as given by :

$$U(x) = \frac{1}{2} K_\theta \left(\theta(x) - \theta_0\right)^2 \tag{3.1}$$

where, in the case of a notch flexure hinge, as shown in fig. 3.2, when rotating by an angle of θ, has a stiffness, as described in Henein (2005), equal to:

$$K_\theta = \frac{2Eb e^{2.5}}{9\pi\sqrt{r}} \tag{3.2}$$

Here, E is the Young modulus of the material, and e,b and r the design parameters of the flexure hinge shown in fig. 3.2.

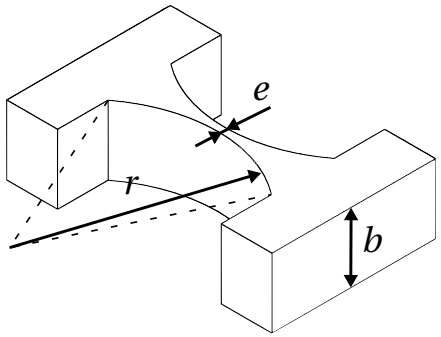

Figure 3.2: A diagram of the notch flexure hinge.

In this approach, the important relationship to obtain is the influence of the contraction of the SMA on the rotation of the hinge, $\theta(x)$. When the flexure-based system is comprised of multiple flexural hinges, the total potential energy can be calculated by the sum of the potential elastic energy of each flexure, $U_{\text{tot}} = \sum U(x)$. The required force to deform the structure can be deduced using :

$$F(\theta(x)) = \|-\nabla U_{\text{tot}}(x)\| = \frac{\partial U_{\text{tot}}(x)}{\partial x} \tag{3.3}$$

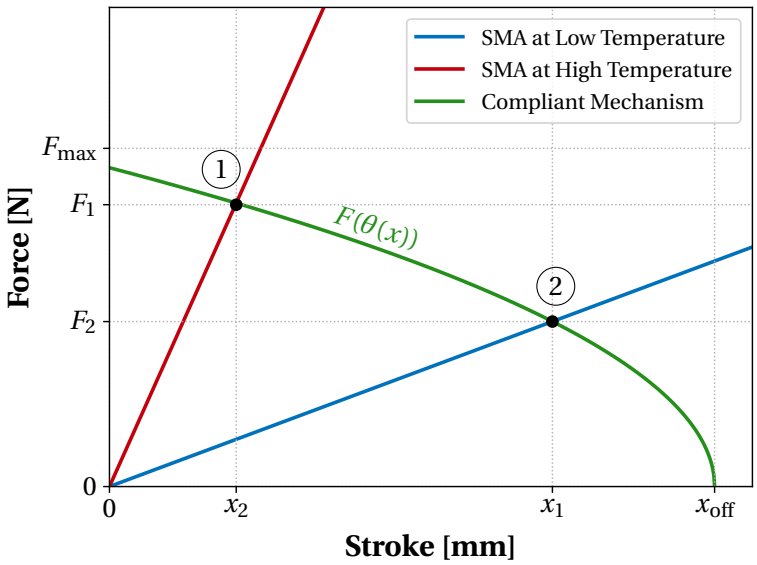

Figure 3.3: The adapted sizing principle of the novel biasing compliant mechanism SMA actuator based on the simplified SMA curves.

As in the case of the traditional SMA sizing methodology, the intersection between the adapted biasing curve and the simplified SMA curves represents the operating points of the SMA actuator, visualised in fig. 3.3 as ① and ②. The stroke of the actuator can be estimated by taking the different between the x-coordinate of the operating points, $\Delta x = x_1 - x_2$. It is important to note that the there is a maximum pull force that the SMA wire or coil can exert, as seen in table cite. Thus, the SMA element must be sized such that $F_1 < F_{max}$ so as to obtain the thinnest SMA wire or coil which can still exert enough force to deform the compliant mechanism to the required stroke.

In fig. 3.4, the design methodology for sizing a biased-compliant mechanism SMA actuator is presented. The methodology consists of designed the SMA active element based on the desired time response (τ) specifications of the application. As explained previously, in the case of passive cooling applications, the wire diameter can be reduced to decrease cooling times and increase τ. Once the diameter of the SMA wire or coil is determined, the biasing element can be designed. In the case of a biasing compliant mechanism, the flexure hinges can be designed based on the desired stroke of the application. As fig. 3.4 details, the operating points must be estimated using the design of the compliant mechanism. The structure and design of the compliant mechanism can be used to determine the relationship between the strain recoverd by the SME and rotation of the flexural hinges, $\theta(x)$. This relationship can be used to determine the force-displacement curve of the resulting biasing element using the equation presented in eq. (3.1). Finally, the individual flexural hinges can be adjusted such that the desired stroke,x, is obtained and that the maximum pull force of the SMA wire or coil is not exceeded.

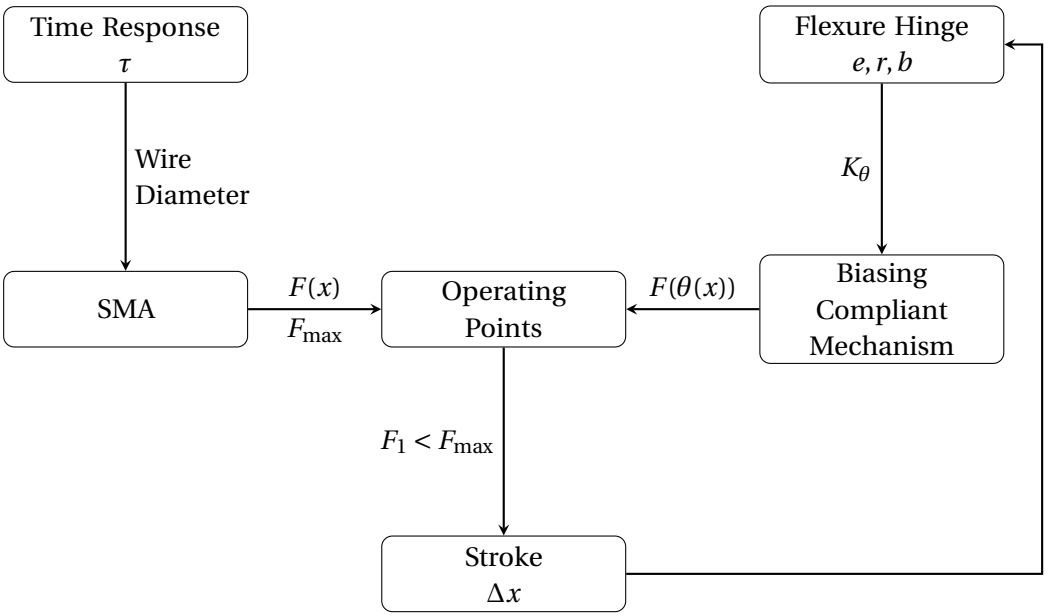

Figure 3.4: Design methodology for sizing biased-compliant mechanism SMA actuators.

Flexure-based hinges, however, exhibit a limited anuglar stroke. The maximum angle allowed before plastic deformation occurs has to be considered when designing such hinges. This admissible deformation, as described in the work by Henein (2005), can be calculated using :

$$\Delta\theta_{\text{adm}} \cong \frac{3\pi\sigma_{\text{adm}}\sqrt{r}}{4E\sqrt{e}} \tag{3.4}$$

By using the relationship between the input displacement and the hinge rotation, $\theta(x)$, the maximum admission stroke of the compliant mechanism, Δx_{adm}, can be computed. With this theoretical model complete, the entire mechanism can be sized such that the output stroke is maximised while avoiding failures during the deformation of the biasing compliant mechanism.

With $\mathbb{X}_{\text{eq}}$ being the set of possible equilibrium positions (see fig. 3.3) and $\mathbb{X}_{\text{el}}$ being the set of admissible positions for elastic deformation as defined below :

$$\mathbb{X}_{\text{eq}} = \{x \mid x_2 \leqslant x \leqslant x_1\} \tag{3.5}$$

$$\mathbb{X}_{\text{el}} = \left\{x \mid x_{\text{off}} - \frac{\Delta x_{\text{adm}}}{2} \leqslant x \leqslant x_{\text{off}} + \frac{\Delta x_{\text{adm}}}{2}\right\} \tag{3.6}$$

The set of feasible operating points for the biased-compliant mechanism SMA actuator, $\mathbb{X}_{\text{f}}$, is given by their intersection:

$$\mathbb{X}_{\text{f}} = \mathbb{X}_{\text{eq}} \cap \mathbb{X}_{\text{el}}. \tag{3.7}$$

Using this principle, if the mechanism is designed such that $\mathbb{X}_{eq} \subseteq \mathbb{X}_{el}$, then, the safety of the flexure hinges will not depend on precise control of the SMA which can be difficult to achieve. Furthermore, using these principle, various design trade-offs can be deduced, as shown in table 3.1

Table 3.1: The trade-offs observed during the sizing of the biasing compliant mechanism for the SMA actuator with a given SMA wire or coil. Here, S_{mech} and t_{mech} are the surface area and the thickness of the compliant mechanism, respectively.

Parameter	Effects	
$\frac{e}{r} \uparrow$	$\Delta\theta_{adm} \downarrow \Rightarrow \mathbb{X}_{el} \downarrow$	$K_\theta \uparrow \Rightarrow \begin{cases} \mathbb{X}_{eq} \uparrow \\ F_{grip} \downarrow \end{cases}$
$e \uparrow \mid \frac{e}{r}$ fixed	$S_{mech} \uparrow$	
$b \uparrow$	$t_{mech} \uparrow$	
$x_{off} \uparrow$	$\mathbb{X}_{eq} \uparrow$, $\mathbb{X}_{el}$ shifted away from $\mathbb{X}_{eq}$	

3.4.2 Integration of Compliant Mechanisms in Antagonistic SMA Actuators

The concept of augmenting traditional bias-spring SMA actuators with compliant mechanisms can be extended to Antagonistic SMA actuators. Traditionally, these actuators consist of a pair of active SMA elements where the SMAs are heated and cooled alternately. These actuators are relatively more complex due to the nonlinear nature of the SME. But, antagonistic SMA actuators have the advantage of an additional degree of freedom during activation. As the first SMA is heated, the antagonistic SMA is deformed and activated. Similarly, only upon heating the antagonistic SMA will the actuator be actuated in the opposite direction.

As with most SMA actuators fabricated using SMA wires or coils, the actuation of the actuator results in a linear motion. In application where complex motions are required, the antagonistic SMA actuator is paired with a kinematic stage that converts the linear movement to the required complex motion. Furthermore, they can be implemented into these antagonistic SMA actuators such that they present different behaviours based on the direction of actuation. As mentioned previously, flexure-based kinematic stages have the advantage of increased precision and reduced weight but presents with an inherent stiffness. Thus, this increased rigidity must be taken into account when sizing the SMA active elements.

In the traditional antagonistic SMA actuator, the first SMA, when heated and returns to its original length, deforms the antagonistic SMA. Thus, in this case, the heated SMA must overcome the rigidity of the cold SMA. The operating points of such a system can be deduced by taking the intersections between the hot and cold SMA curves as shown in chapter cite. In the case of a compliant mechanism, the system is connected to both SMAs at all times. Thus, the inherent stiffness of the compliant mechanism must be taken into account when actuated both SMAs. Therefore, the force-displacement curve of the compliant mechanism, $F_C(x)$, can be added to the curve of the antagonistic cold SMA, $F(x)$, to obtain the apparent

load observed by the heated SMA, as shown in fig. 3.5. The design methodology can thus be adjusted, as shown in fig. 3.6, such that when the SMA elements are sized and operating points are determined, no unintended behaviours occur. It is important to note that due to the complexity of the compliant mechanism curves, these unintended operating points can emerge causing shorter strokes.

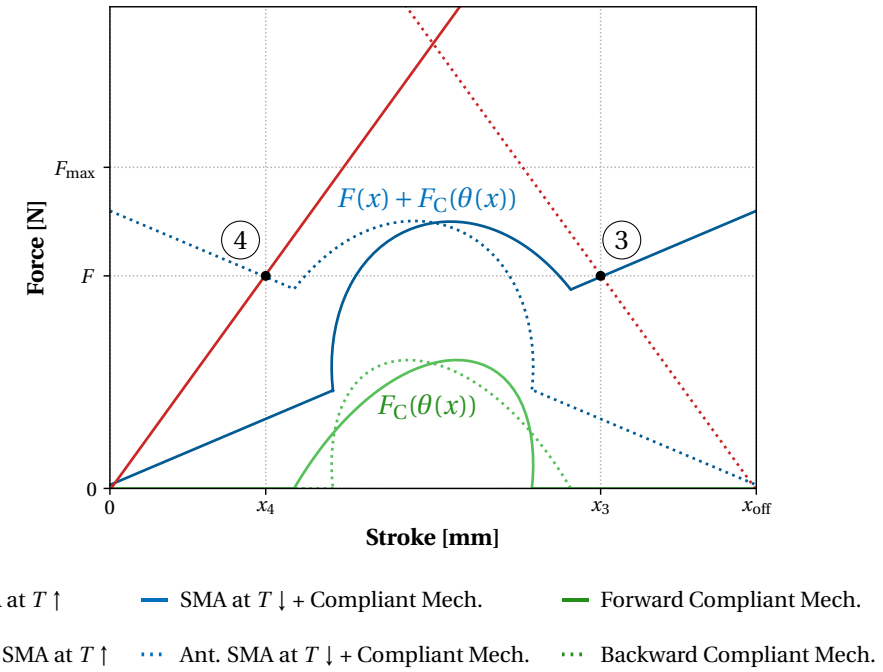

Figure 3.5: The adapted sizing methodology of an antagonistic SMA actuator paired with compliant mechanism using the simplified SMA curves.

In summary, as illustrated in fig. 3.6, the design methodology consists of deriving the force-displacement curves of the SMA elements and the relationship between the input displacement, x, and the hinge rotation, $\theta(x)$. Once these relationships are deduced, the force-displacement relationship of the compliant mechanism, $F_C(\theta(x))$ can be added to the force-displacement curve of the cold antagonistic SMA element. An important parameter to note is the prestretched length, x_{off} of the SMAs. As the SMA is prestretched, when heated, the SMA can exert higher levels of force but could result in forces that exceed F_{max}. Using the two curves, the operating points can be estimated and verified such that the resulting stroke, Δx, fits within the requirements of the application. Furthermore, the geometric parameters of the hinge design of the compliant mechanism can be adjusted such that there are no unintended operating points and that the maximum pull force of the SMA is not exceeded.

Recently, there has been considerable work in developing bistable or multistable actuators. These actuators are able to main a stable position without required any holding energy. This property could be highly beneficial in applications such as grippers. Here, the gripper can stay in the open or closed position without requiring any additional energy. These bistable systems

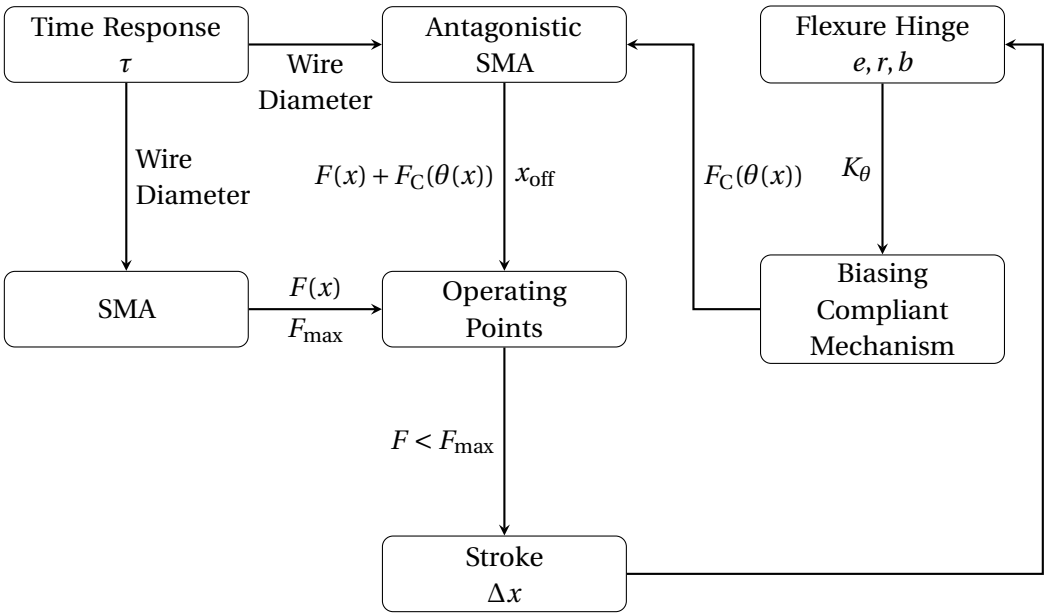

Figure 3.6: Design methodology for sizing antagonistic SMA actuators paired with compliant mechanism.

can be created using flexure-based structures, as shown in the work by Jin Qiu et al. (2004). A axially compressed cantilever beam exhibits bistability and has been implemented in various smart material actuators. In the work by Chouinard and Plante (2012), a dielectric elastomer actuator is paired with a buckled beam to create a compact bistable actuator. Furthermore, in the work by Zhang et al. (2020), a bistable drone-ready gripper is fabricated and is actuator using an electric motor. This principle can be implemented and actuated using SMAs, as shown in the work by Welsch et al. (2018). However, the sizing of such a system are missing due to the complex nature of the bistable mechanism and the nonlinear nature of the SMA. Using the proposed, methodology, as shown in fig. 3.6, the SMA can be sized to present with higher time responses while still able to trigger the bistable positions of the actuator. The accurate sizing of such a bistable SMA actuator is validated later in section 6.3.

3.5 Summary and Conclusion

In this chapter, the traditional sizing methodology has been adapted to fit the case where biasing springs are replaced with passive biasing compliant mechanism. This approach stems from the concept where the traditional SMA actuators consisting of an active element, a biasing element and a kinematic stage is transformed into a more integrated solution where the biasing element and the kinematic stage are combined.

Using pseudo-rigid body models described in the work by Henein (2005), the analytical models of the compliant mechanisms are used to estimate the stroke and behaviour of the novel SMA actuator. Using the simplified SMA curves, these alloys can be sized such that the time

response of the SMA actuator is minimized.

Furthermore, this novel approach to designing SMA actuators paired with compliant mechanisms has been adapted for antagonistic SMA actuators. By altering the design methodology, the often used antagonistic SMA actuators can be sized such that when paired with compliant mechanisms, the actuator does not present any unintended behaviours and reduces the time response.

Most SMA actuators that make use of kinematic stages to convert the linear motion of the actuator into more complex behaviours, also integrate a passive spring in the design. By applying the presented design approach, SMA actuators can be designed such that compliant mechanisms can be used as biasing elements. This methodology will be further validated using case studies in chapter 6.

4 Designing Actuators Powered by Compliant SMA Elements

4.1 Introduction

Smart materials, due to their integrated nature of reacting mechanically to a certain type of stimulus, have become an integral part of designing complex actuators. These materials have become an integral part of designing integrated and compact actuators. As presented in chapter 3, integrating the traditional building blocks of the tradition smart actuator can results in more compact designs. The behaviours of smart materials, however, range from simple linear behaviours to highly complex multi-physical behaviours. Thus, designing smart actuators with complex geometries are only feasible with certain types of smart materials.

In the case of shape memory alloys, the shape memory effect is a complex non-linear behaviour that is reliant on multiple kind of physics. This results in active elements present in SMA actuators to often be in the shape of wire, coil or thin sheets. These 1-dimensional structures are the most common type of implementation in SMA actuators due to the fact that their behaviours when heated or cooled are more easily predicted. As stated, in practice, when complex motions are required, the actuator is composed of complex kinematic stages and a simple SMA wire or coil as shown in the work by cite.

When taking inspiration from other more established smart materials, complex designs that still exhibit the smart behaviours of the material are often generated using algorithm as shown in the work by cite. Topology Optimization (TO) has been essential in designing such complex design that can take simple inputs and transform them into more complex and useful outputs. These compliant mechanisms fabricated from smart materials are compact and lightweight. However, combining this design methodology with SMAs can be quite difficult and computationally expensive to implement due to the highly non-linear nature of the Shape Memory Effect (SME).

In this chapter, a robust design methodology to design compliant SMA structures for powering integrated smart actuator is presented. Furthermore, a qualitative factor is described that can be used to compare various generated SMA topologies. Using Finite Element Modelling

(FEM), the various topologies are simulated and shown to exhibit the shape memory effect.

4.2 Designing Integrated Active Elements

When designing smart actuators that display complex output motions, they generally consist of 1D SMA structures such as wires coupled with complex kinematic stages that transform the simple linear motion into complex ones, as shown in the work by citeand cite. By extrapolating the methodology presented in chapter 3, it is conceivable to imagine a scenario where the active SMA elements and the kinematic stages are combined, as shown in fig. 4.1. Here, compliant structures fabricated from a monolithic block of SMA can be used to create compact actuator that no longer require a kinematic stage consisting of multiple pieces.

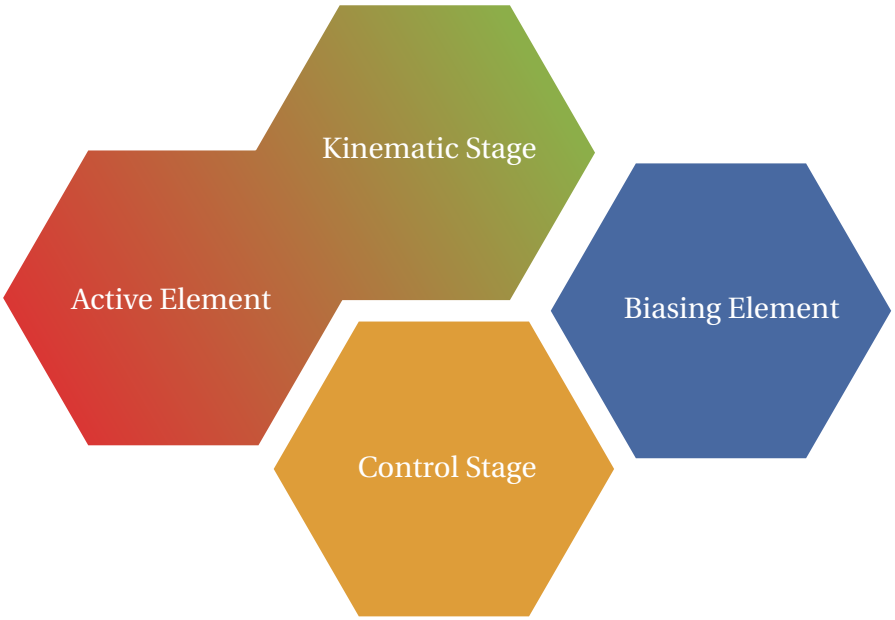

Figure 4.1: Diagram of the adapted building blocks of the SMA actuator based on integrating the active element and the kinematic stage.

The challenges posed by this approach consist of the complex nature of the shape memory effect. The behaviour, consisting of highly non-linear behaviour and comprised of multi-physical variables, makes it hard to predict when the complex geometries are heated or cooled. Furthermore, implementing generative algorithms that design these complex geometries, as implemented with other simpler smart materials, is difficult due to the high computational costs required to simulate the shape memory effect.

4.3 Designing with Topology Optimization

Due to the high computational costs of simulating the shape memory effect, it is quite difficult to generate complex novel geometries even with poor mesh resolution. The basic principle of the proposed approach is to generate novel designs made of SMAs with computer-aided methods such as topology optimisation method (TOM). Here, the crux of the approach consists of abstracting the temperature-dependent effects but appropriately formulate the design problem so as to indirectly take into account the requirements of the shape memory effect.

When purely optimising for strain and assuming a standard elastic material, compliant mechanisms can be designed without considering the nonlinear nature of the material. Here, as mentioned previously, the requirements of the shape memory effect consists of a certain level of deformation during lower temperatures. Thus, the optimisation, when designing the compliant structure that when exposed to a biasing element, prioritises the strain across the entire structure. As long as the material undergoes sufficient deformation, above a critical strain threshold, will exhibit the shape memory effect when heated to higher temperatures. The analysis is executed assuming small and purely elastic deformation to reply on linear finite element analysis so as to significantly reduce the computational time.

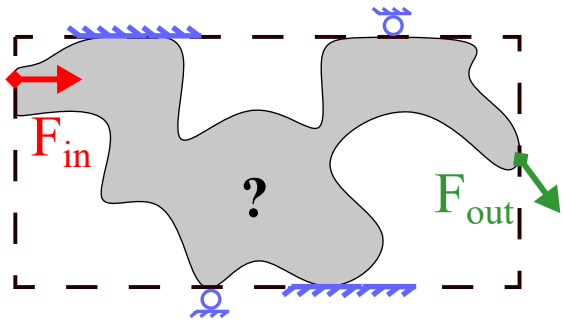

Figure 4.2: Basic design problem for compliant mechanisms.

4.3.1 Density-Based Topology Optimization

The basic concept being topology optimisation consists of investigating the distribution of material inside a discretised design space while trying to improve a certain specified objective function. The design variables applied in this density-based approach optimisation are artificial densities ρ that describe the proportion of the material, $0 < \rho_{\min} \leq \rho \leq 1$, an individual domain space is filled with. The lower and upper bounds of density range are considered as *full* materials representing fully empty or fully filled elements, respectively. While the densities within the range are defined as *intermediate* materials. Here, this artificial density variable are made continuous to use a gradient-based solver which has the advantage of lower computational time compared to non-gradient based approaches, as shown in the work by Sigmund (2011). In order to avoid mesh-dependent solutions and checker-board patters, the optimisation is regulated. This is achieved with a density filter that limits the length scale, $r_{\min}$,

to a minimum inside the structure, as shown in the work by Bendsoe and Sigmund (2013).

Each iteration of the optimisation consists of the following steps. First, the filtered design variables are mapped to a material property using the Material Interpolation Scheme (MIS). This converts the artificial densities into a usable Young's Modulus. Next, the well-known Solid Isotropic Material Penalisation (SIMP), as shown in eq. (4.1) from the work by Bendsoe and Sigmund (2013), is implemented. This scheme penalises intermediate materials so as to prevent obtaining a geometry that cannot be manufactured. This is done using a penalty facor n which continuously increases throughout the optimisation.

$$\mathrm{E}_e = \mathrm{MIS}(\rho_e) = (\overline{\mathrm{E}} - \underline{\mathrm{E}})\rho_e^n + \underline{\mathrm{E}}, \tag{4.1}$$

with $\underline{\mathrm{E}}$, $\overline{\mathrm{E}}$ the lower and upper bound of $\vec{\mathrm{E}} = [\mathrm{E}, \cdots, \mathrm{E}_{\mathrm{NE}}]^{\mathrm{T}}$ respectively corresponding to the Young's modulus of an "empty" element and a completely filled one. NE is the number of elements inside the domain. When the material properties of each element are known, the *Stiffness matrix* K of the corresponding structure is constructed. Next, Finite Element Analysis (FEA) is performed to estimate the displacement U of each node under imposed external loads F so as to solve the linear elasticity equation: KU = F. The chosen objective function with its associated sensitivity (gradient of the objective function with respect to the design variable) is evaluated using these, aforementioned, displacements. For the following iteration, the sensitivities can, then, be used by the solver to update the design variables. In this case, the Optimality Criteria (OC) scheme from the work by Bendsoe and Sigmund (2013) is used as the solver.

One of the main advantages to this approach to designing compliant SMA elements is the fact that various Open-Source academic codes are available for implementing this structural topology optimisation as shown in the work by Zhu et al. (2020) and Talischi et al. (2012). Due to ignoring the thermal dependencies of the shape memory effect, the resulting FEA used is similar to that of traditional compliant mechanisms and can thus be easily extended to such generative algorithms by simply changing the objective functions and associated sensitivity.

4.3.2 Topology Optimization of Compliant Mechanisms

The basic principle behind designing a compliant mechanism, as illustrated in fig. 4.2, can be formulated as : "Under an external input force and certain boundary conditions, what is the distribution of material defining the compliant mechanism that transforms the input load to a specific output one?"

At the input and output points, artificial springs are added to simulate the input work and resistance to the output displacement of the workpiece, respectively, as shown in the work by Alonso et al. (2014). In the final geometry, these springs are removed and are only present during the design process. Regarding the objective function that governs the final design of the compliant mechanism, a formulation that can be extended to Multi-Input Multi-Outputs

(MIMO), is implemented based on various strain energies as shown in the work by Alonso et al. (2014).

An objective function based upon the mutual strain energy between the input and output is chosen. This permits to distribute the strain throughout the structure and avoid to have only *de facto* (single point) hinges responsible for the compliant behaviour. Ideally, the maximum volume of the structure should be deformed to harvest as maximum work, when the alloy is heated and experiences the shape memory effect. Here, the objective function is built using three different types of strain energies. First, there is the input strain energy S_{in}, that is present when only an input load F_{in} is applied and result in some nodal displacements U_{in}. Similarly, the output strain energy S_{out}, is present when only a dummy unit load F_{out} is applied at the output port resulting in nodal displacements U_{out}. Finally, the Mutual Potential Energy (MPE) or mutual strain energy S_{mut} can be built with the two previous nodal displacements. The objective function is chosen as a ratio of these three energies due to its non-dimensional aspect and due to the fact that the desired input and output displacements are indirectly accounted for. Here, since the problem is formulated as a minimisation, a minus signed is placed before the chosen ratio to maximise the MPE as follows :

$$\gamma = -\frac{S_{mut}}{S_{in} + S_{out}} = -\frac{{U_{out}}^T K U_{int}}{\frac{1}{2}{U_{out}}^T K U_{out} + \frac{1}{2}{U_{in}}^T K U_{in}}. \tag{4.2}$$

Lastly, two separate FEAs are performed to evaluate the chosen objective: $KU_{in} = F_{in}$ and $KU_{out} = F_{out}$.

The current objective governing the design of the generated compliant mechanisms made of *conventional* linear material, can be extended to generating design for mechanisms made from SMAs. This is due to the fact that, as previously mentioned, the algorithm tends to distribute the strain throughout the structure which will indirectly allow a large portion of the material to be activated if made from SMA. The optimisation problem, as formulated in eq. (4.3), consists of the minimisation of the objective function γ subject to the limitation of the infill Vol^* of the design domain's volume, with V_e the volume of element e.

$$\begin{aligned} \min_{\vec{\rho}} : \quad & \gamma(\vec{U_{in}}, \vec{U_{out}}, \vec{E}) \\ \text{s.t. :} \quad & KU_{in} = F_{in} \\ & KU_{out} = F_{out} \\ & Vol < Vol^*, \text{ with } Vol = (\sum_{e=1}^{NE} \rho_e \cdot V_e)/(\sum_{e=1}^{NE} V_e) \\ & \vec{E} = MIS(\vec{\rho}) \quad 0 < \rho_{min} \leqslant \rho \leqslant 1. \end{aligned} \tag{4.3}$$

In fig. 4.3, the basic design problem is displayed using the common force inverter scenario.

Due to the symmetry of the problem, the domain space can be restricted to half the surface while adding rolling supports at the symmetry axis. In fig. 4.4, the evolution of the optimisation can be observed. Here the domain space is uniformly initialised with intermediate materials such that the volume limitation is satisfied so as to have the design converge to a solution that is only composed of full materials.

4.4 Testing using Benchmark problems

Before designing complex multi-output compliant SMA elements, the shape memory effect of the generated geometries must be validated. In this regard, a common practice is to use some traditional benchmark problems. The problems, while being simple problems, can be used to validate the generated designs using a commercially available Finite Element Modelling (FEM) software such as ANSYS®. Using an FEM, the shape memory effect of the generated topologies can be simulated, verifying the efficiency of the algorithm for designing compliant SMA mechanisms.

The proposed design method is applied to three benchmark problems : an inverter, a crimper, and a gripper. They are all fixed at their bottom and top left corners (which corresponds to ideal pivots) but each have their own input and output forces. The design problems and the resulting geometries are shown in fig. 4.3, fig. 4.5, and fig. 4.6. This half domain space has been discretised into 10^4 elements and the design variables are initialised uniformly with a volume fraction constraint of 30%. The stiffness of each artificial spring is equal to 0.1 and the input forces are equal to 1. When run on a Windows workstation with an Intel i7 3.6 GHz, 8-core processor and 32 GB of memory, the complete process takes less than 1 minute to converge to solution. It is important to note that the computational time would have been significantly higher if a non-linear and multi-physic analysis was executed. Due to the short computational time, this design method can be extended to 3-Dimensional problems.

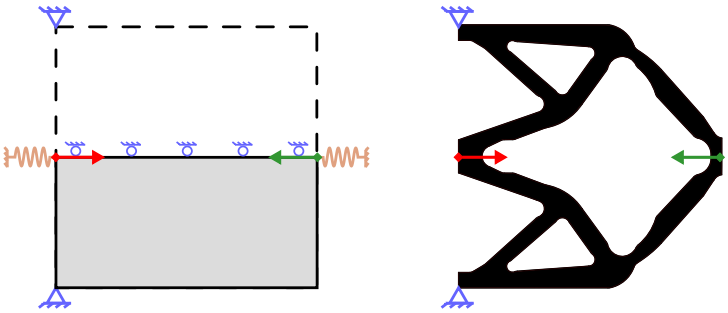

Figure 4.3: Inverter: Design problem (left), Interpolated final topology (right). Input force is shown in red while the output force is shown green.

Here, in the hopes of validating the shape memory effect, a four time-step simulation is constructed. The four different simulated steps can be seen in fig. 4.7. Here, the figures represent the results of the FEM simulation for each benchmark problem. The simulation

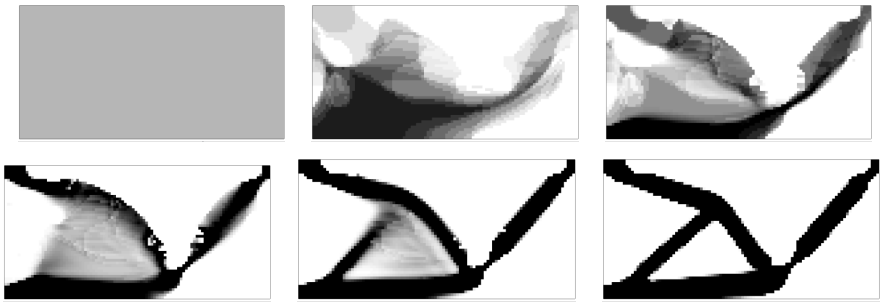

Figure 4.4: Evolution of the inverter design throughout the optimization. The grayscale represent the value of the filtered artificial density.

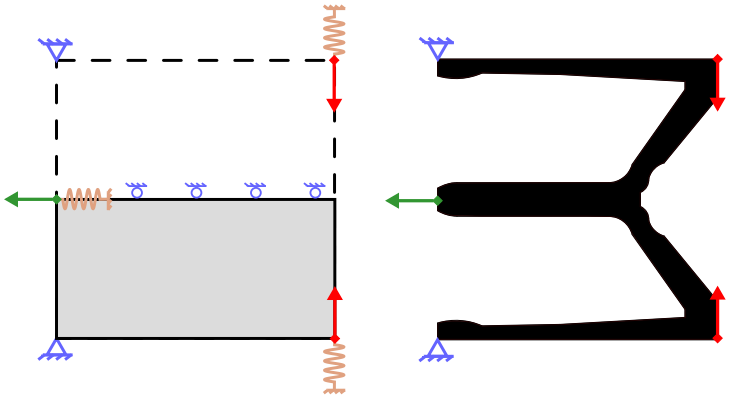

Figure 4.5: Crimper: Design problem (left), Interpolated final topology (right). Input force is shown in red while the output force is shown green.

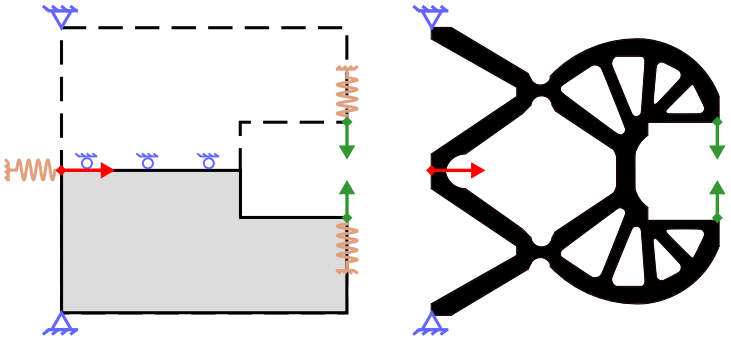

Figure 4.6: Gripper: Design problem (left), Interpolated final topology (right). Input force is shown in red while the output force is shown green.

consists of first applying an input displacement which generates a displacement at the output, $\varepsilon_{\text{loaded}}$. If the entire structure is sufficiently strained to undergo the detwinning process, as explained in chapter cite, the structure will keep its deformed shape when the input displacement constraint is released. However, as some areas of the compliant structure does not undergo detwinning, a portion of the strain will be lost when the constraint is released. Thus, the observed strain at the output will decrease to $\varepsilon_{\text{free}}$. During the third time step, the

structure is heated to activate the shape memory effect and force the structure to revert back to its original shape where all the strain is recovered. Finally, the structure is allowed to cool down and return the material back to its martensitic phase.

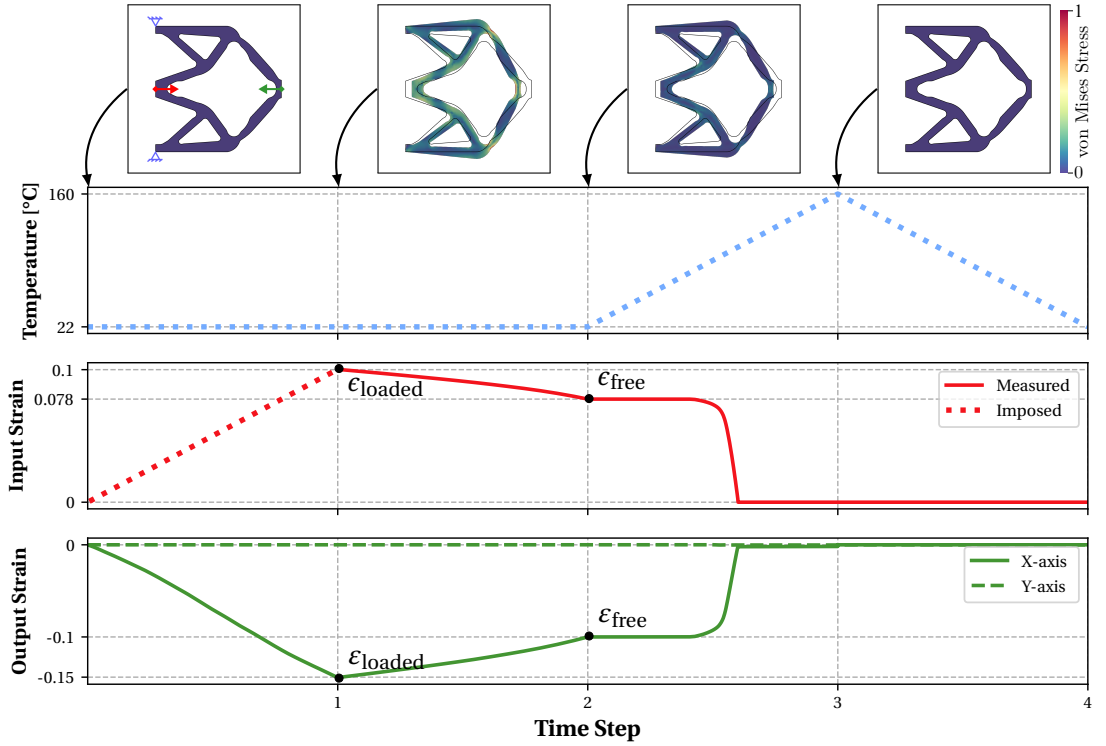

Figure 4.7: Results of the shape memory effect simulation of the Inverter design. Here, the displacements are calculated relatively to the design domain size L. The displacements observed between time steps 1 and 2 show a strain retention of $\alpha_\epsilon = 77.6\%$ confirming the presence of the shape memory effect.

4.4.1 A Qualitative Measure of the SME

Since the topologies generated by the algorithm are widely different consisting of varying inputs, outputs and geometries, a measure by which the results can be compared is required. The final goal, being to integrate these compliant mechanisms as the active element in a biased-spring SMA actuator, the measure should represent the degree to which work has been stored by the biasing element. This measurement factor could be formulated as a measure of the relative quantity of material activate (or detwinned) by the biasing element. This implies that the larger the value of the factor is, the more optimal the biased-actuator will perform.

The amount of detwinned material in the geometry can be roughly estimated using the principle that the deformed material behaves plastically. In other words, it is the volume of the material that is able to retain its shape after the load has been released. This factor, as described in eq. (4.4), is expressed as the strain retention factor and is defined as the amount

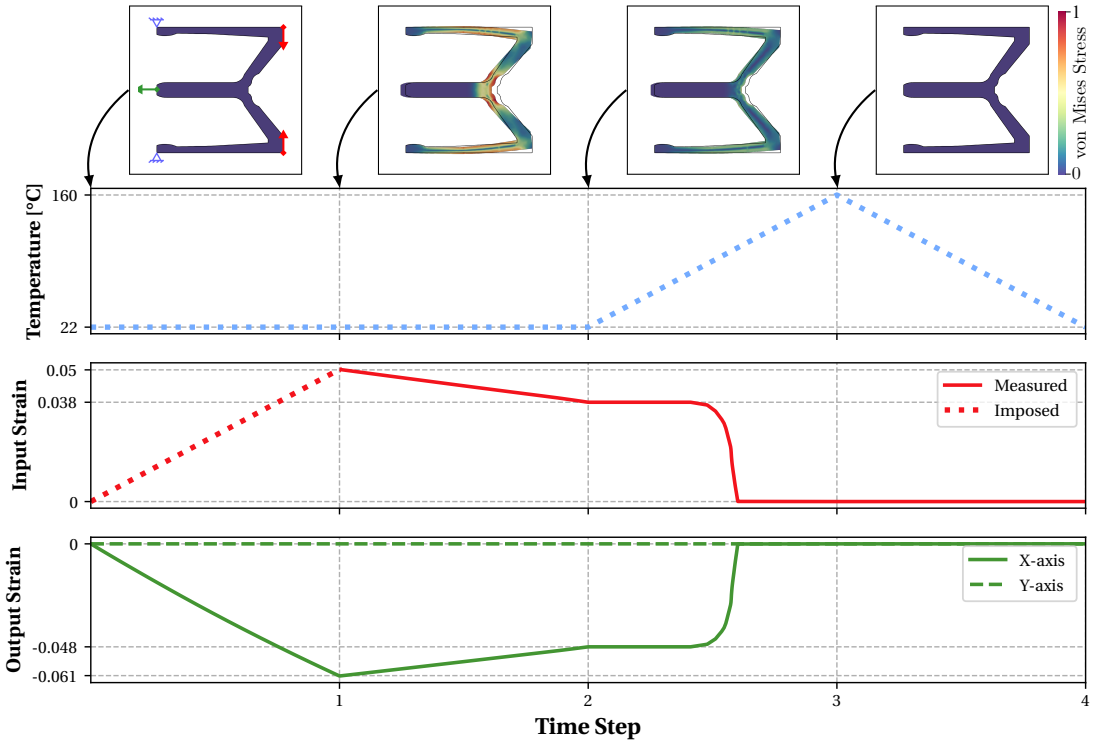

Figure 4.8: Results of the shape memory effect simulation of the Crimper design showing a strain retention of $\alpha_\epsilon = 75.2\%$.

of strain observed in the topology after the deformation load is released. This factor will vary between 0 implying non of the material has been activated and the topology retains completely back to its original shape when the load is released and 1 for a perfectly detwinned material where the entirety of the strain is retained and can only be reverted back to its original shape when heated. This strain retention factor can be calculated using :

$$\alpha_\epsilon = 1 - \frac{\epsilon_{\text{loaded}} - \epsilon_{\text{free}}}{\epsilon_{\text{loaded}}}, \tag{4.4}$$

with ϵ_{loaded} and ϵ_{free} representing the domain space normalised input displacement at time step 1 and 2 respectively. It is important to note that this factor can never be equal to 1 as there is some natural elastic spring back of the material even when fully detwinned and thus, is only a qualitative measure of the shape memory capabilities of the topology. It is still an effective way to compare the different topologies presented using the benchmark problems. The FEM results of the strain retention of each benchmark problem can be seen in table 4.1. This principle can be further extended to more complex designs where goal is to create compliant SMA structures that can have multiple outputs using just a single input biasing element which will be presented in future sections.

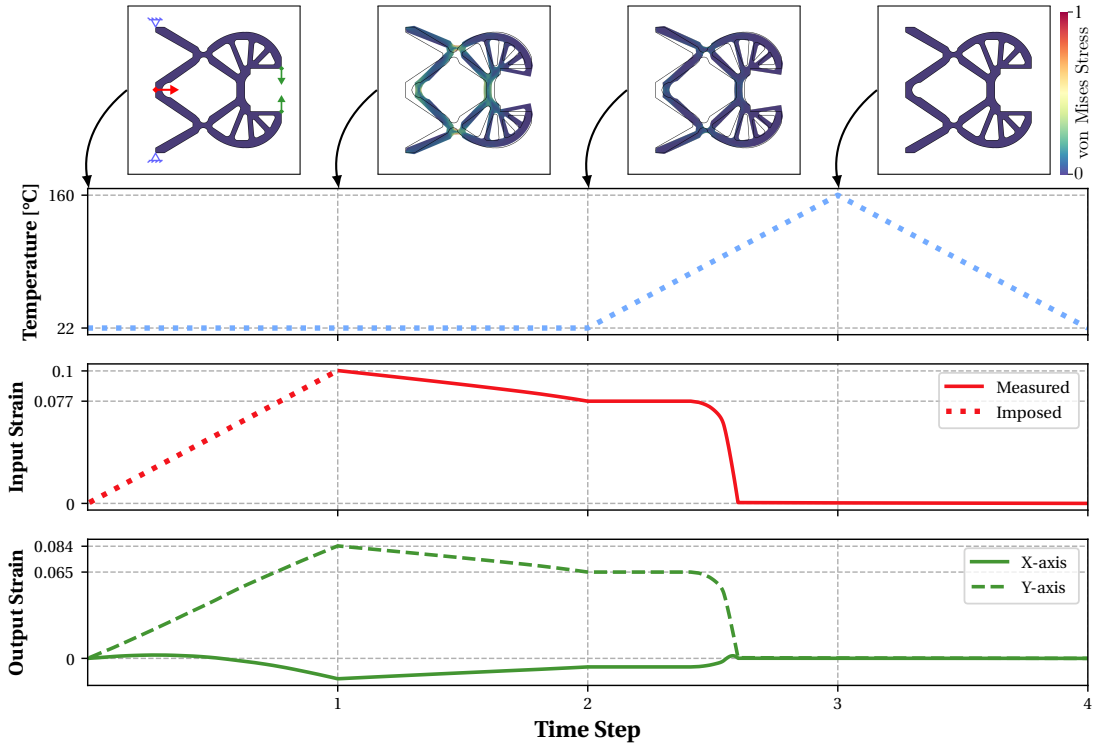

Figure 4.9: Results of the shape memory effect simulation of the Inverter design showing a strain retention of $\alpha_\epsilon = 77.6\%$.

Table 4.1: The simulation results of the strain retention factor for each of the benchmark problems: $\mathscr{I}$ Inverter; $\mathscr{C}$ Crimper; $\mathscr{G}$ Gripper

	$\varepsilon^x_{\text{loaded}}$	$\varepsilon^y_{\text{loaded}}$	$\varepsilon^x_{\text{free}}$	$\varepsilon^y_{\text{free}}$	α^x_ϵ	α^y_ϵ
$\mathscr{I}$	0.149	-	0.103	-	**77.6%**	-
$\mathscr{C}$	−0.061	-	−0.048	-	-	**75.2%**
$\mathscr{G}$	0.015	−0.085	0	−0.065	**77.6%**	-

4.4.2 Experimental Validation of the Methodology

In the previous section, three benchmark problems were used to validate the presence of the shape memory effect of topologically optimised compliant structures made from SMAs. Furthermore, a qualitative measure was formulated so as to compare and assess the degree to which these compliant structures would be ideal in creating biased-spring SMA actuators. However, to truly verify the presence of the shape memory effect, an experimental prototype can be fabricated.

For an accurate comparison between the FEM results and the experimental data, a prototype of a benchmark problem is conceived. For the sake of simplicity, the inverter problem is chosen

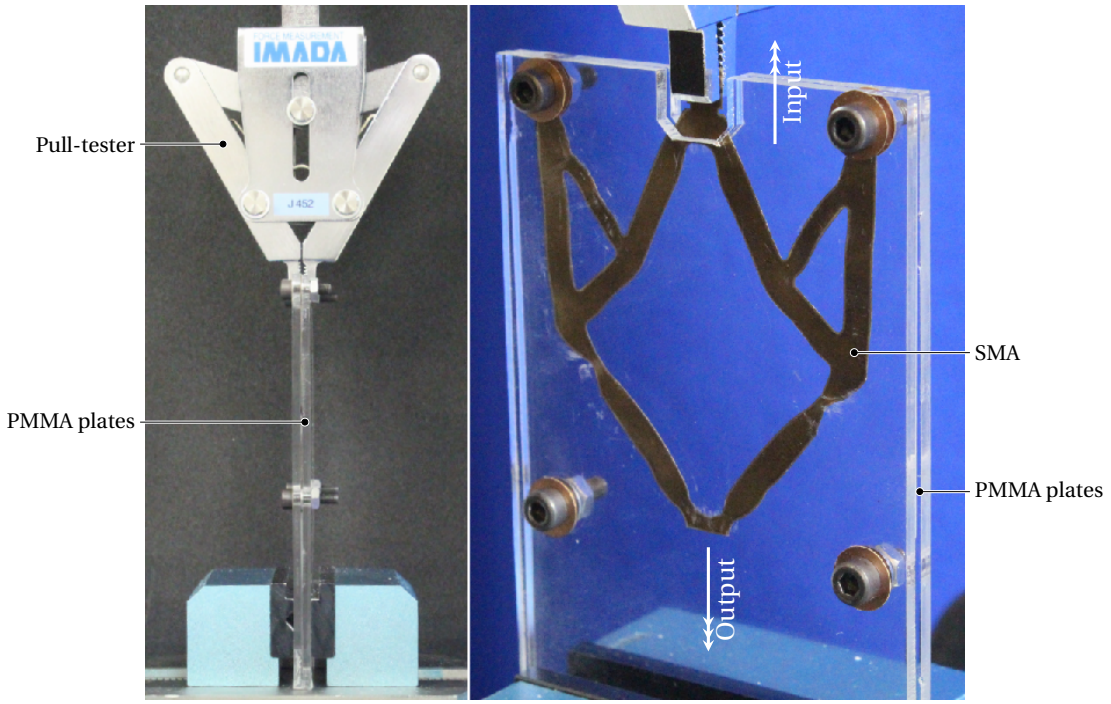

Figure 4.10: The experimental setup of the inverter prototype. The prototype is cut from a thin SMA sheet and is sandwiched between PMMA sheets to prevent buckling. The input load is applied using the pull-tester while measuring the input displacement and force. The output displacement is recorded using a microscopic camera.

due to the fact that there is only one input and output. When designing the inverter, ideal pivots are used. However when creating the experimental prototype, these ideal pivots are changed to a more realistic solution involving mounting holes. Based on these new boundary conditions, the inverter problem is redesigned using the proposed topology optimisation algorithm.

When fabricating the prototype, the cost of machining a monolithic block of NiTiNOL was deemed unfeasible. With the advent of additive manufacturing of NiTiNOL as portrayed in the work by cite, the creation of such compliant mechanisms has become cheaper and more feasible. However, in this case, as the topology generative is 2-Dimensional, the inverter prototype was fabricated by laser cutting thin sheets of NiTiNOL (55.8 wt. % Ni). This laser cut inverter structure was then sandwiched between two PMMA sheets to prevent any unwanted buckling in the third dimension, as shown in fig. 4.10. This ensures that the deformations observed within the structure resembles the simulation.

The advantages of such a implementation, to test the validity of the design methodology, include the reduced cost of the prototype and more importantly, ensuring that the stress and strain distribution within the 2D structure is identical to the simulated 3D structure. This implies that the output displacement of the inverter prototype will closely resemble that of the simulated structure. The main disadvantage of this implement comes from the

fact that the PMMA sheets cause lots of friction with the compliant structure. This implies that force requirements at the input will be higher than expect. As we sandwich the PMMA sheets more tightly around the compliant structure, the output displacements will be more accurate while increase the friction and force requirements to create the aforementioned output displacement. Thus, a trade-off is present but the strain retention factor, as described in eq. (4.4), is only dependent on the the displacement and not the force requirements. Thus, the prototype was fabricated to maximise the input and output fidelity rather than the force requirement. Here, a pull-tester is used to measure the displacement of the input and the force requirements.

The goal of this section is to experimentally validate the proposed design methodology. The prototype of the compliant SMA benchmark problem was realised and must be compared to the results of the simulation. As described before, the strain retention factor was developed to compare the various generated topologies and to have a qualitative analysis of the structure to be used as a bias-spring SMA actuator. Thus, this factor can also be used to compare the experimental prototype of the modified inverter mechanism and its corresponding FEM simulation.

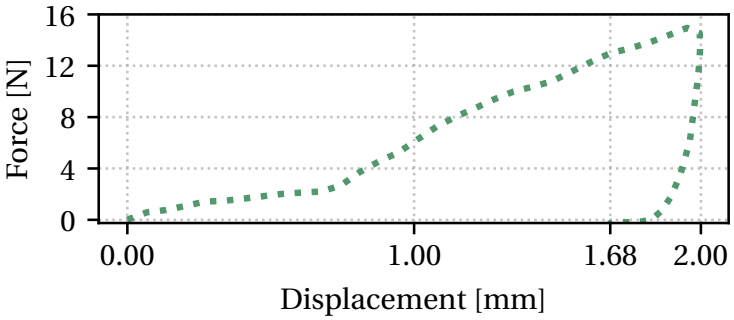

Figure 4.11: The experimental results of the inverter prototype are obtained using a pull-tester and a strain retention of 84.3% is observed.

In fig. 4.11, the pull-tester results can be seen. The strain retention is measured by applying an initial strain to the input of the prototype using the pull-tester. By then reversing the direction of the pull-tester and measuring the reaction force, the point at which the reaction force descends below 0 N will define the strain that is retained by the structure after the initial load is released. We assume that as the pull-tester observes a value below -0.2 N, the structure has overcome the internal friction with the PMMA sheets and is now bending the input of the prototype rather than returning to its original shape. Based on the values observed using the pull-tester, a strain retention of 84.2% is measured as shown in table 4.2. When comparing to the results of the simulation of the same modified inverter topology of 78.9%, the shape memory effect capabilities of topologies generated by this design approach is validated. The difference in the strain retention between the experimental and FEM results can be accounted by the friction present in the physical implementation.

Table 4.2: Comparison between the FEM and experimental results of the modified inverter benchmark problem.

	x_{loaded} [mm]	x_{free} [mm]	α_ϵ [%]
FEM	2.0	1.58	78.9
Expt.	2.0	1.68	84.3

4.5 Proposed Induction Heating Strategy

Due to the complex geometries of the generated topologies, simply passing a current through the structure by attaching electrode to the ends is no longer possible. In the case of inverter prototype, electrodes must be attached at multiple points so as to allow current to flow through all the areas of the geometry.

Various works have been established where surface mounted coils have been installed to function as a heating coil that raise the temperature of the SMA structures for localised heating, as shown in the work by cite. This can be quite cumbersome due to possible risks of delamination while the SMA contracts and dilates during actuation. Another option would be to use hot air as a medium to increase the temperature of the SMA structure, perhaps with tools such as hot air guns. These external heating structure drastically reduce the work density of the resulting actuator and are thus, rarely used in small and compact applications.

Due to the complex geometry of the inverter prototype, the current paths for Joule's heating are no longer unique, nor trivial anymore. Here, in this case, multiple electrodes with multiple external wires are required to heat the structure. Thus, here, the proposed heating solution consists of a contactless, wireless strategy where a current is induced within the SMA structures using external induction coils.

4.5.1 Magnetic Induction Heating

The basic working principle of the proposed heating methodology and its application in the inverter mechanism can be seen in cite. By passing an alternating current at a high frequency is passed through the primary coil and generates a magnetic field. When any electric conductor, the SMA structure in this case, is placed inside the generated magnetic field, a secondary electric current, I_{induced}, is induced inside the structure. This induced current will generate Joule's losses, P_{Joules}, heating the SMA :

$$P_{\text{Joules}} = R_{\text{SMA}} \cdot I^2_{\text{induced}} = \frac{V^2_{\text{emf}}}{R_{\text{SMA}}}. \tag{4.5}$$

The magnitude of the current is based on the electromotive force, V_{emf}, generated by the primary coil, and the effective resistance, R_{SMA}, of the path taken by the induced current. The

coupling between the primary coil and the SMA piece, as described in eq. (4.6), dictates the electromotive force.

$$V_{\text{emf}}^2 = \left(-\frac{d\Psi}{dt}\right)^2 = \left(-2\pi f L \cdot I_{\text{prim}}\right)^2 \tag{4.6}$$

where Ψ is the total flux linkage between the primary and SMA side, f is the working frequency, I_{prim} is the *RMS* value of the primary current and L is the mutual inductance between the primary coil and the SMA structure. As a voltage source is used to power the system, the input current is maximised and the resistance of the primary coil is minimised. This is further increased by creating a resonating circuit where a capacitor is connected to the primary coil.

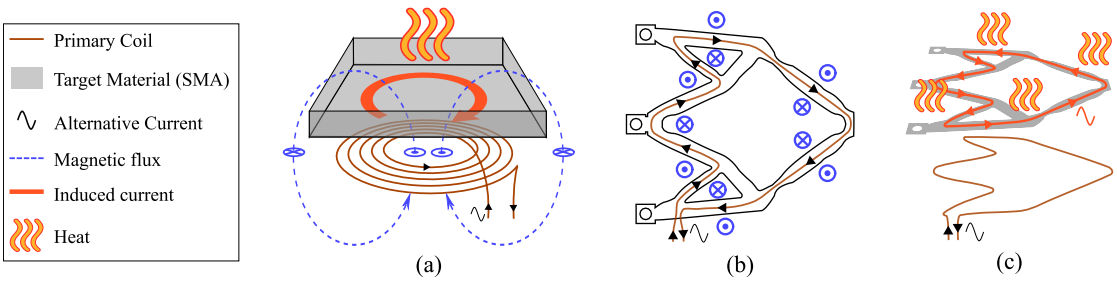

Figure 4.12: Induction heating - (a) General principle, (b) 2D view of the coil designed for the deformed inverter, with the direction of the generated magnetic flux normal to the plane, (c) 3D view of the induction system for the inverter problem.

When designing the heating solution for maximum induced current, as shown in eq. (4.6), a large working frequency is desired. However, when working with alternating currents at high frequencies, undesirable effects such as skin and proximity effects, arise which increase the resistance of the primary coil. Furthermore, the parasitic capacitance of the impedance of the coil will take over above a certain critical frequency, cancelling the inductive effect. By limiting the working frequency, a favourable balance between the losses at the primary coil and the induced current at the resonant value can be maintained. The mutual inductance between the primary coil and the SMA structure can be maximised for a large area of influence and a large number of turns. However, the area of influence cannot be increased as it is constrained by the shape of the generated SMA topology while the number of turns is limited by the associated increase in resistance which in turn reduces the magnitude of the input current. Thus, based on the application, the sizing of the primary coil comes with various trade-offs.

4.5.2 Fabrication and Results of Primary Coil

Due to the complex shape of the generated SMA topologies, the shape of the primary coil must be designed so as to induce a current path across the deformed regions of the compliant mechanism. Currently, the fabrication of the primary coil is performed by hand using nails and a wooden plate. The nails are used to create the shape based on the desired current path and a wire is wound around the nails to fabricate the coil. Once constructed, varnish is used to maintain the shape of the primary coil when the nails are removed. As shown in fig. 4.13, two types of primary coils are constructed using 25 turns a standard monolithic wire with a

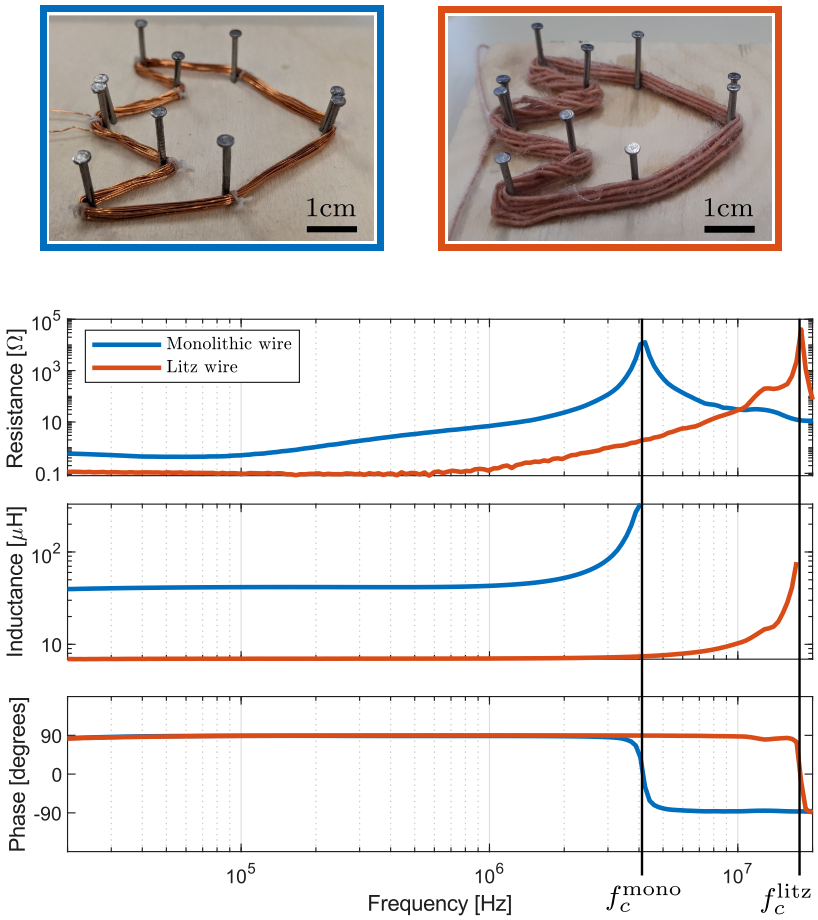

Figure 4.13: Comparison of primary coil with different types of wire. As the impedance becomes mainly capacitive over its critical frequency, the inductance's values after $f_c^{\text{mono}} =$ 17MHz and $f_c^{\text{litz}} = 41$MHz are removed for the monolithic and Litz wire respectively.

copper diameter of 0.30mm, and another composed of 15 turns of a Litz wire composed of 300 strands with a diameter of 0.040mm each. As shown in fig. 4.13, the resistance of tbe wire increases significantly with the frequency due to the skin and proximity effects. This implies that a thinner effective cross-section is preferred, as in the case of the Litz wire.

As mentioned previously, the working frequency plays an important role in this proposed heating system. A trade-off is present where a higher value increases the heating but also increase the parasitic capacitance of the coil, limiting the impedance above a critical frequency, $f_c^{\text{mono}} = 17$MHz and $f_c^{\text{litz}} = 41$MHz for the coil made of monolithic and Litz wire, respectively. As shown, despite the lower inductance of the Litz coil, better heating performance is achieved due to the working frequency and higher primary current when compared to the monolithic wire.

Here a working frequency of around 4 Mhz has been chosen so as to ensure that it sits safely above the critical frequency. At this frequency, the inductance of the coil is $L = 7.4$ μH and its

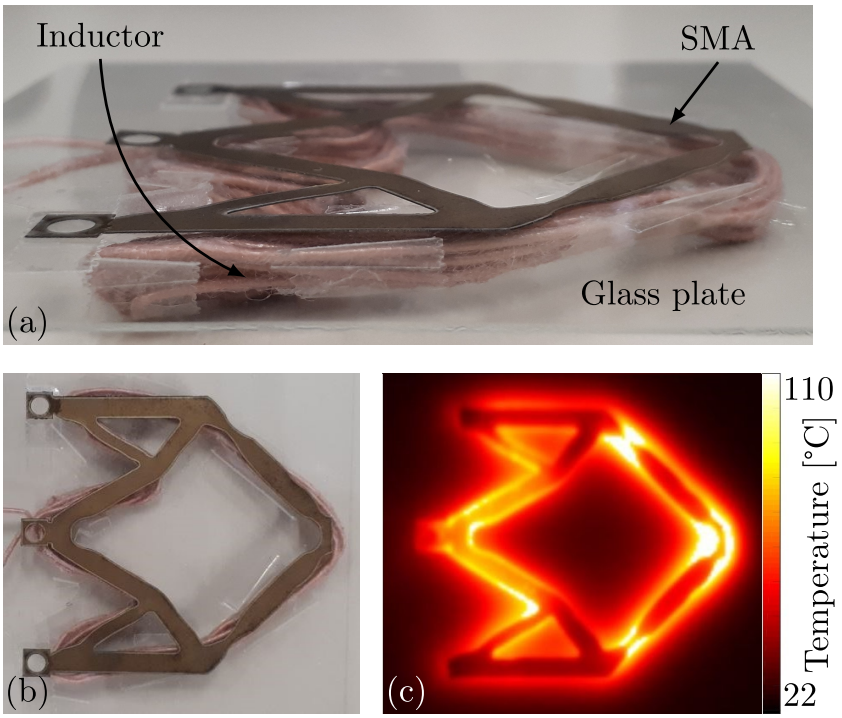

Figure 4.14: Implementation of induction heating system. When activated, it resulted in the heating of the SMA structure, reverted the deformed structure back to its original shape.

resistance $R = 0.4\ \Omega$. A capacitor of $C = 230$ pF is attached in series with the primary coil to create an LC circuit with a resonating frequency $f = (2\pi\sqrt{LC})^{-1} = 3.86$ MHz. Here, the input source is constructed using a half-bridge inverter based on GaN transistors (EPC9024). With the Litz coil, a primary current of $I = 1.5$ A is generated at the working frequency while dissipating 0.9 W of heat. This increased temperature is negligible and implies a stable operation. However, the coil made from the monolithic wire would result in higher temperatures at the primary resulting in a change in resistance and inductance values.

The fig. 4.14 illustrates the implementation of the contactless inductive heating system for the compliant SMA prototype as well as the temperature distribution across the SMA structure using the FLUKE® Ti25 thermal camera. A glass plate is placed between primary coil and the SMA to avoid any heating through convection. Using the proposed heating system, the SMA inverter prototype was heated above 120°C validating the system as an active heating system. Furthermore, as the structure reverts back to its original shape, this further validates the presence of the shape memory effect.

In this implementation of the prototype, the penetration depth does not limit the excitation frequency as the structure is composed of a thin film of SMA. In the case of a working frequency of 10 MHz, the penetration depth is larger than the 100 μm thick SMA sheet. However, in a real world application where the compliant structure is created from a thick monolithic block of SMA or 3D printed, the penetration depth would be an additional parameter to account for

when sizing the input frequency.

4.6 Designing Multi-Output Compliant SMA Actuators

The proposed design methodology consisting of using topology optimisation to design compliant SMA mechanisms was validated using a FEM simulations and experimental results using standard benchmark problems. Furthermore, as the generative design algorithm used made abstraction of the shape memory effect, the designs of the compliant mechanisms were generated with a relatively low computational time. Due to the cost of NiTiNOL and advanced manufacturing techniques, prototype of the proposed design could not be fabricated but advanced additive manufacturing methods that avoid waste of material such subtractive methods such as machining has become possible as shown in the work by citeand cite. With these techniques, complex compliant SMA actuators could be fabricated in the near future. Thus, the proposed design methodology could be a great tool in creating novel biased-spring SMA actuators.

4.6.1 Generated Multi-Output SMA Actuators

In this section, various novel multi-output actuators fabricated from compliant SMA topologies are generated based on the proposed design methodology. These topologies were, similar to the benchmark problems in section 4.4, simulated and their corresponding strain retention factors were measured, as shown in fig. 4.16. The *rhombus* structure is a multi-directional mechanism where the axes move in opposing directions. They elongate in the y-axis and contract in the x-axis. The other structures, named the 8-*point mandrel*, the 4-*point mandrel* $\times$ and the 4-*point mandrel* +, perform as outer-mandrels for gripping objects. The evolution of the topology during the generative optimisation process for the 4-*point mandrel* $\times$ is shown in fig. 4.15. In a similar way to the benchmark problems, these topologies are generated while making abstraction of the shape memory effect and while neglecting the nonlinear nature of the alloy so as to drastically reduce the computational time, which took less than 2 min per design.

Using the FEM simulation of these multi-output compliant mechanisms and the strain retention factor, the presence of the shape memory effect within the generated topologies is validated. A fixed input strain of 10% is applied at each input, where the bias-spring is attached, to have comparable results for each design. The results of the FEM simulation of the design are presented in table 4.3. The obtained strain retention factor for each actuator topology shows that the majority fo the strain applied by the biasing spring is retained and will be recovered when heated using the proposed induction heating methodology. This implies that this design methodology could be an attractive tool for designing novel multi-output biased-spring SMA actuators.

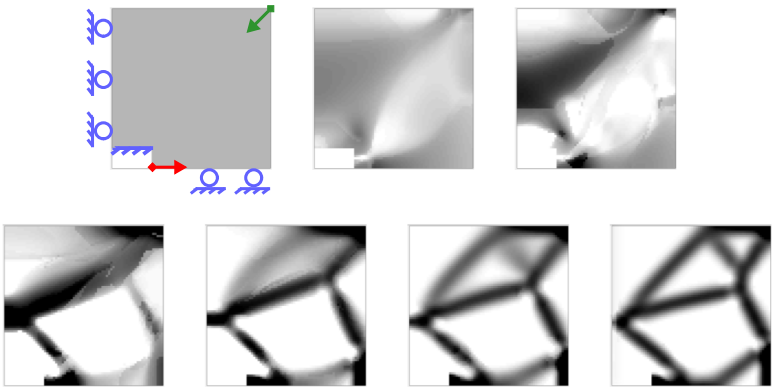

Figure 4.15: 4-point Mandrel × : Evolution throughout the optimization. The grayscale represents the value of the filtered artificial density. The input force is shown in red and the output force in green.

Table 4.3: Comparison between the FEM and experimental results of the modified inverter benchmark problem.

	$\varepsilon^x_{\text{loaded}}$	$\varepsilon^y_{\text{loaded}}$	$\varepsilon^x_{\text{free}}$	$\varepsilon^y_{\text{free}}$	α^x_ε
Rhombus	①: 0.051 ②: 0	①: 0 ②: 0.062	①: 0.042 ②: 0	①: 0 ②: 0.045	**67.9%**
8-Point Mandrel	①: -0.057 ②: -0.057 ③: 0	①: 0 ②: -0.05 ③: -0.085	①: 0.037 ②: -0.038 ③: 0	①: 0 ②: -0.034 ③: -0.058	**74.7%**
4-Point Mandrel ×	-0.029	-0.022	-0.023	-0.017	**81.4%**
4-Point Mandrel +	①: 0.051 ②: 0	①: 0 ②: 0.062	①: 0.042 ②: 0	①: 0 ②: 0.045	**68%**

4.7 Kirigami inspired Compliant SMA Actuators

Using topology optimization, various compliant SMA actuators can be designed with the intent to combine the functions of the kinematic stage and the active element. However, due to the current limitations of fabrication and its costs, the feasibility of such an actuator, in the current sense, is unlikely. As additive manufacturing of SMAs becomes more accessible, the

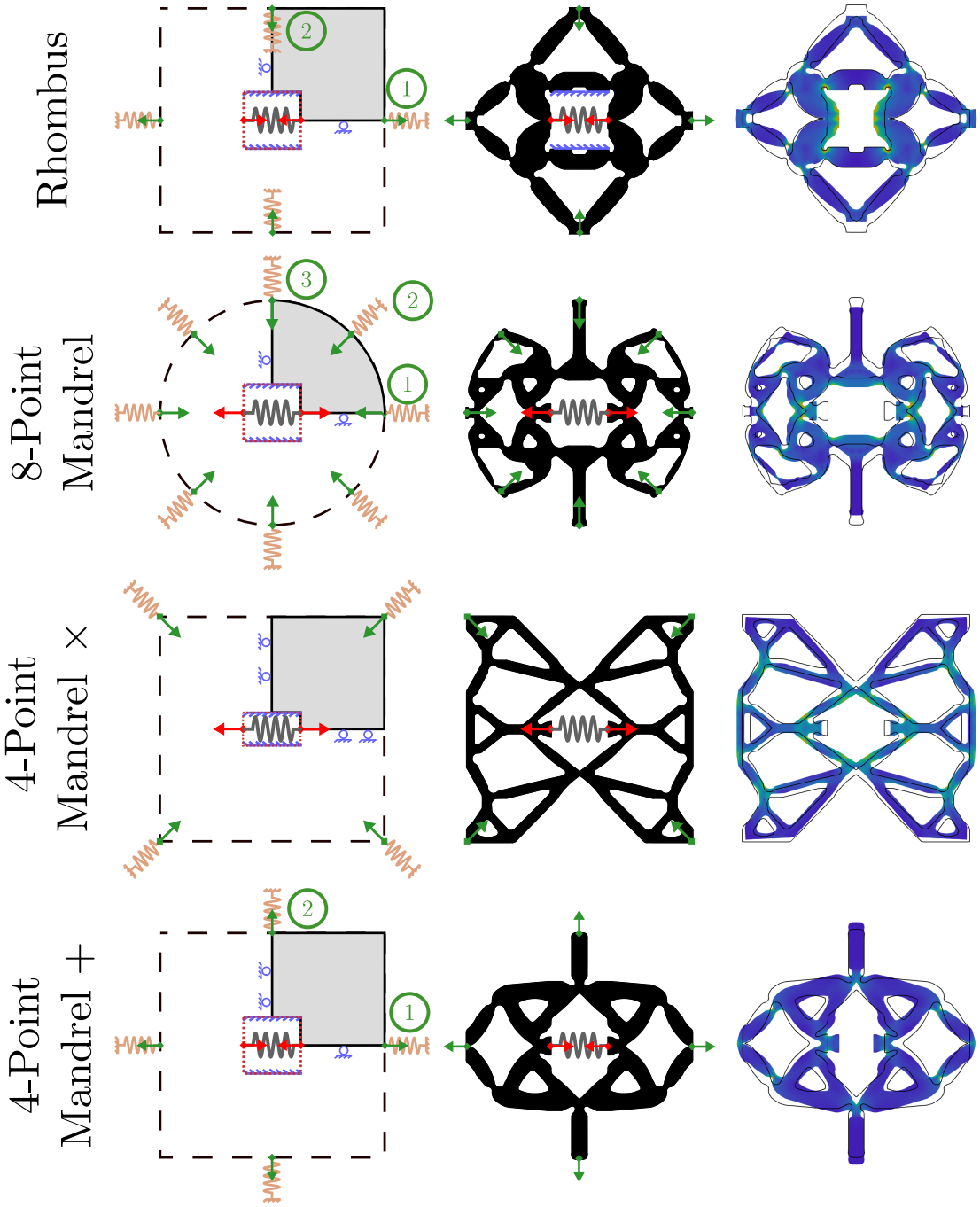

Figure 4.16: Using the novel design methodology, multi-output bias-spring SMA actuators are generated making use of compliant SMA structures, shown with normalised stress distribution in the deformed state. The input forces are shown in red and the output forces in green. The artificial springs present in the topology optimisation are shown in brown while the bias-springs of the actuators are shown in grey.

advantages of designing compliant SMA structures such as increasing the overall work density of the actuator, will become more apparent and attractive.

Kirigami, the Japanese art of cutting paper to create intricate structure, has gained traction in various engineering fields to create stretchable structure as shown in the work by cite. While designing 3D compliant structure made of SMA is expensive, this kirigami approach can be extended to SMAs to create compliant structures that when cut in a specific manner, can exhibit surprising mechanical behaviours.

When designing actuators, a key detail to keep in mind is the life cycle of the device. In common industrial applications, the number of cycles to fatigue of traditional grippers can exceed 10^6 cycles. In the case of SMA actuators, this number is much lower and is directly related to the structural fatigue of the material. The determining factors regarding the fatigue life of SMAs are the strain amplitude and the type of strain applied to the material. The work by Runciman et al. (2011) looks at the fatigue lifetime of NiTiNOL based on different loading conditions, such as torsion, tension and bending. They conclude that SMAs tend to have a much longer life cycle when loading under torsion or bending when compared to tension. The results show that with a fixed strain amplitude of 1%, in tension, the number of cycles to failure is less than 10^3 whereas in bending or torsion, the number of cycles to failure is around 10^5.

The availability of NiTiNOL in different geometries such as springs, wires and sheets, has allowed the creation of multiple classes of SMA actuators that exploit their respective advantages. As mentioned in previous sections, the simplest approach would be to use the alloy in the shape of a wire paired with a biasing spring to drive an actuator where the stress and strain of the material corresponds directly to the stroke and force output of the actuator. In these cases, SMA wires are elongated under pure traction and are then heated to recover the strain and provide the force output as shown in the works by Kyung et al. (2008), Welsch et al. (2018), Haibin et al. (2018), and Andrianesis and Tzes (2015). Here, the stroke of the actuator can not exceed 1% without compromising its fatigue life. Thus, in cases where a larger stroke is required, the geometry of the wire is adapted to form a spring which can provide stroke above 100% as implemented in the works by Ikuta (1990) and Zhakypov et al. (2018). Here, the material no longer deforms in traction but rather in torsion, thereby increasing its fatigue life but while compromising the force output. This implies that there is a trade-off to be made between the force output, and the stroke and fatigue life.

Since SMAs are available in the form of sheets which can be machined using laser cutters into complex geometries, different kinds of SMA actuator systems exploit the longer fatigue life of SMAs in flexion to create novel grippers as shown in the works by Kohl et al. (2002), Benard et al. (1998), Zhakypov et al. (2018). The major advantage to using sheets instead of wires is the fact that they provide a much higher force output. The difference in force output between sheets and wires can be reduced by placing multiple wires in parallel to generate forces in the same order of magnitude as sheets. Thus in applications, where a higher force output is

required, the use of SMA sheets or multiple wires in parallel can be a viable solution.

When working with thin wires, placing them in parallel to augment the overall force output also increases the complexity of the system greatly. The manufacturing and assembly of such a system can be difficult. Furthermore, it is also impossible to uniformly deform all the wires equally, resulting in some wires being inactive during the shape memory effect. Thus, in cases where a higher force output is required, the design space can become limited to just using sheets. For maximum force output, the sheet can be elongated in pure traction but only up to about 1%. In applications where a large stroke and force output is required, the SMA sheets in its original state is no longer viable. Traditionally, this limitation is overcome by adding a kinematic stage to amplify the stroke of the SMA actuator but comes with the cost of reduced overall work density of the final actuator.

In this section, a novel approach will look at a new kirigami-based approach to designing SMA sheets to obtain an actuator that can provide higher force output while being able to also provide high strokes. Kirigami is a variation of origami that involves the cutting of the substrate to create different shapes and behaviours. The pattern presented in this paper is based on the work by Shyu et al. (2015) where a nanocomposite substrate is patterned to create a stretchable element. This approach allows an SMA sheet to reach strains over 100% without losing its capacity to deliver a high force output.

4.7.1 Proposed Patterns

4.7.2 Implementation

4.8 Summary and Conclusion

In this chapter, a design methodology, consisting of integrating the kinematic stage and active element to create a compact SMA actuator, is proposed. Using topology optimization and a novel approach to generate topologies while making abstraction of the shape memory effect is detailed. By implementing such a generative algorithm, the computational time to design novel topologies has been drastically reduced. This has the implication to extending such a design algorithm to 3D structures.

The design approach using topology optimisation was tested using benchmark problems with a standard input and output parameters to create various topologies that can be fabricated from SMAs. The presence of the shape memory effect and the feasibility of the topologies to be used in SMA actuators was validated using a FEM simulation and an experimental prototype. Furthermore, a qualitative measure called the strain retention factor was proposed as a means to compare the various topologies that can be generated using such an approach.

As these novel structures can be complex, the heating of such geometries using simple Joule's heating is no longer trivial. A novel heating solution was proposed and fabricated so as to activate the shape memory effect of the fabricated topologies. Furthermore, using this design

approach and generative design algorithm, various multi-output biased-spring SMA actuators, that can be actuated using only a single biasing spring, were proposed.

These SMA structures were designed within a 2D space with the intention of fabricating the structure from a 3D monolithic block of SMA. As the design algorithm was implemented with a volume constraint to preserve material, fabricating the structure with subtractive methods such as machining will result in large amounts of wasted material. However, due to the current cost limitations of additive manufacturing processes that exist for SMA, the feasibility of such a compliant SMA structure is limited.

Lastly, the same methodology where structure composed of complex patterns that exhibit surprising mechanical behaviours, can be be seen in kirigami-inspired structures. By extending this same design principle to SMA actuators, patterns can be cut into thin SMA sheets such that high stroke actuators can be fabricated without the need for cumbersome external kinematic stages.

Using this design principle, compliant SMA active elements can be designed and fabricated so as to appropriate the functions of the kinematic stage within the SMA actuator. This allows for the creation of compact SMA actuators that retain their high work energy density.

5 Integrating Control Systems into SMA Actuators

5.1 Introduction

Shape Memory Alloys, often referred to as artificial muscles, are often used in applications where a compact and lightweight solution is required. When paired with a biasing element such as a spring or compliant mechanism, a lightweight reversible actuator can be fabricated. By heating and cooling the active SMA element, a reversible back and forth motion can be created.

Due to the complex nature of the shape memory effect, sensors or complex control strategies are required for the accurate control of the SMA element, as shown in the work by citeand cite. The SMA, if overheated, can result in the permanent reprogramming of the shape or the destruction of the SMA wire or coil. In the case of smaller, more compact applications, the SMA element used are thin wires or coil. In these cases, using sensors that can measure the temperature can be quite difficult to implement due to the low thermal mass of the SMA element. Recent work such as cite, have implemented sensorless systems where the change in resistivity is measure as the SMA changes phase to create more compact control solutions. Here, due to the complex nonlinear nature of the shape memory effect requires complex control strategies and micro-controllers to efficiently control the SMA and prevent overheating.

Often, when considering the volumetric work density of SMA actuators, the electronics, sensors and control strategies are not taken into account. In certain applications, for example untethered crawling robots, the control plays an important role in the final work-weight density of the robot as seen in the work by cite. Improvements made in the sensorless and control strategies can, thus, have a major impact in the final dimensions and weight of the SMA actuator.

In this chapter, a novel design concept is presented to further integrate the discrete building blocks present in the traditional SMA actuator. By exploiting the dependence of the mechanical behaviour of the SMA and its temperature, a mechanical oscillator system can be developed

such that an electronics-free SMA actuator can be designed. This design language can be implemented into SMA actuators to create a simple but effective solution to create a sensorless, micro-controller-free control strategy that intrinsically present SMA overheating. Furthermore, in this chapter, a crawling robot is conceived using this methodology to validate this novel design approach.

5.2 Design Methodology for the Control System

As mentioned previously, due to the complex behaviour of SMAs, the sensors and control strategies required to actuate an SMA actuator can be cumbersome and reduce the overall work-weight density of the resulting robotic systems. The shape memory effect and the corresponding phase transitions are directly dependant on the temperature of the alloy. By exploiting this mechanical relationship between the temperature of SMA, the control system can be integrated into the kinematic stage, as represented in fig. 5.1.

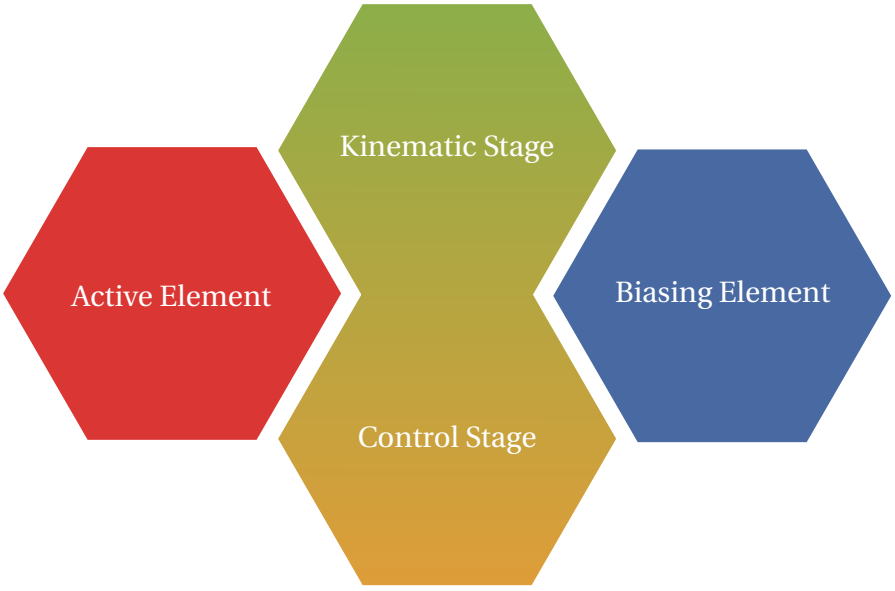

Figure 5.1: Diagram of the adapted building blocks of the SMA actuator.

5.2.1 Working principle

A basic linear SMA actuator consists of an SMA and a biasing spring that when heated and cooled, results in a simple back forth oscillating motion. By accurately controlling the temperature of the SMA above its transition temperature and below a critical overheating temperature, the SMA can be made to provide a reliable actuation. This reversible actuation results in a back and forth mechanical movement of the biasing spring and the cyclical movement of the kinematic stage, if any. The basic concept of this methodology consists of tying the mechanical behaviour of the actuator into the control.

The SMA element in most cases is heating using Joule's heating by simply passing a current through the SMA and allowing the internal resistance of the SMA element to heat up by Joule's losses as shown in the work by cite. The cooling of the SMA generally consists of passively extracting the heat from the active element using natural convection with the cooler surrounding air. This simple strategy is often used in the control of SMA actuators due to not requiring any additional mechanisms and thus, does not reduce the work-density of the actuator while keeping the system compact.

Thus, by using the mechanical behaviour of the actuator to cut the current flow across the SMA will immediately cool the active element before it has a chance to overheat. In this manner, the control of the SMA actuator is mechanical controlled by the shape memory effect. Here, as a current is passed through the SMA wire or coil, it heats up the SMA resulting in a strain recovery and the SMA returning to its original length. This change in length, after a certain threshold, can be made to physically cut the electrical contact between the SMA element and the power supply. This cause the immediate cooling of the SMA through heat exchange with the surrounding air. As the SMA cools down, the biasing element will, once again, deform the SMA which will re-establish the electrical contact across the SMA, restarting the oscillating motion. Thus, this design strategy when integrated into the kinematic stage can render the entire SMA actuator compact and electronics-free.

This approach, when properly implemented, can result in an robotic system where a reversible actuation can be observed without the need for any electronics, micro-controllers or sensors, preserving the work-weight density of the system. A mechanical control of the SMA element can result in a system where the SMA element, due to the physical electrical contacts being interrupted, can never overheat.

5.2.2 Implementation

The basic implementation of such as system consists of using a latch system or multi-stable mechanism where after a certain stroke or force threshold results in a snap-through effect that can be exploited to disconnect the electrical contacts across the SMA wire or coil. The rapid bifurcation or spring back from a latch system is used to cut the flow of current across from the SMA and the slow return of the SMA actuator due to cooling can be used to re-establish the electrical connection to create this oscillating effect.

The implementation of this oscillator mechanism in the scope of a simple biased-spring SMA actuator consists of a magnetic or mechanical latch system. A diagram of the working principle of the proof-of-concept can be in fig. 5.2. The latch, here, consists of a magnet mounted on a leaf spring that is attracted to the end-effector of the bias-spring SMA actuator. The electrical current, in this case, is made to flow across the conductive magnet and into the SMA coil. Thus, only as the the magnet attaches to the end-effector of the SMA actuator will the SMA coil be heated using Joule's losses. Essentially, as the magnet and the SMA coil makes contact, the SMA element is heated and reduces in size due to the shape memory effect. During this

phase, the magnet, which is mounted to a leaf spring, experiences a return force, F_S, and will continue to follow the actuator. Once, this force exceeds the attractive magnetic force, F_{mag}, between the magnet and the SMA coil, the latch detaches and immediately returns to its original location. This spring back occurs due to the resting return force of the leaf spring attached to the magnet. This concept can be implement in numerous ways including a mechanical latch mounted on a passive spring. Once this snap-through occurs, the electrical connection and the electrical current across the SMA is cut and will only be re-established when the bias spring of the SMA deforms the SMA coil and extends it back towards the latch. In this manner, the oscillating behaviour is observed without any sensors, micro-controllers or electronics.

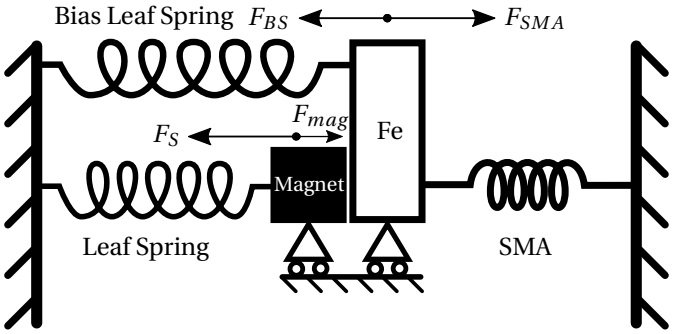

Figure 5.2: Diagram showing the working principle of the magnetic latch system implemented in the SMA oscillator.

As mentioned earlier, using a flexure-based mechanism permits the omission of a dedicated spring in the design. As seen in fig. 5.3, a proof-of-concept of this design methodology is implemented. Here, the linear stage is comprised of two parallel cantilever beams that also behaves as leaf springs. These biasing leaf springs apply a tractional return force on the SMA coil at a lower temperature while also preventing any unwanted degrees of freedom in the other axis. Another leaf spring is used to apply the return spring force required in the magnetic latch. Here, the SMA actuator is heated using the magnetic latch system and the snap-through of the latch occurs when the return force of the leaf spring exceeds the attractive force of the magnet, $F_S > F_{mag}$. Therefore, the required contraction of the SMA coil, ε, can be controlled by sizing the leaf spring associated with the magnet.

$$\varepsilon = \frac{F_{mag}}{K_s} \tag{5.1}$$

where K_s is the rigidity of the leaf spring which depends on the dimensions of the cantilever beams and can be calculated using the analytical model described in the works by Rubbert et al. (2016) and Henein et al. (1998).

Here, in this proof-of-concept, the magnetic latch consists of a small magnet, with an attractive force of 150 g, mounted on a thin leaf spring measuring 500μm × 2.5mm × 30mm. An M2 screw is used to clamp an electrically conductive wire to the magnet and acts as the ground

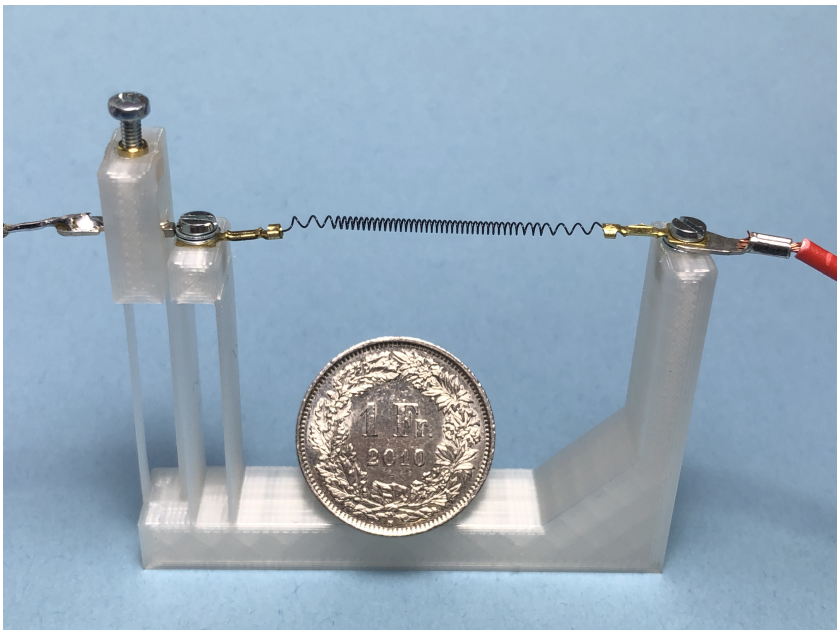

Figure 5.3: The integrated SMA control system implemented using a flexure-based magnetic latch creating an SMA mechanical oscillator.

of the electrical circuit. The magnet latches onto another ferromagnetic M2 screw which is mounted to the end-effector of the SMA actuator, as seen in fig. 5.4. The SMA is supplied by *Dynalloy, Inc* (Irvine, CA) and is a 90°C Flexinol® coil with wire diameter of 200 μm and an outer diameter of 1.4 mm. The coil contains around 40 coils and with a solid length of 8 mm. The SMA is mounted on a 3D printed support containing a flexure-based linear stage which supports the free end of the SMA. The linear stage is 3D printed from PLA and consists of 2 parallel leaf springs with dimensions 500 μm x 10 mm x 30 mm.

This basic concept can be implemented in using different methods. The latch system can be replaced by a bistable mechanism and can then be paired with antagonistic SMA actuators. Here, the control system can be linked to the snap-through of the bistable mechanism where each stable position controls the heating of each SMA element. In this way, the first SMA can be heated till the snap-through of the bistable mechanism which will then change the electrical contact across the antagonistic SMA. This concept has been implemented and validated in section 6.3.

5.2.3 Sizing of the oscillator

As mentioned previously, the thermomechanical behaviour of the SME is exploited to create the mechanical control system. The sizing of the oscillator system is, thus, directly, dependant on the thermal properties of the active element. The rise time or time till the snap-through occurs, depends on the time required to heat the SMA using Joule's heating. This implies that the current supplied across the SMA dictates the rise time of the oscillator. The fall time or

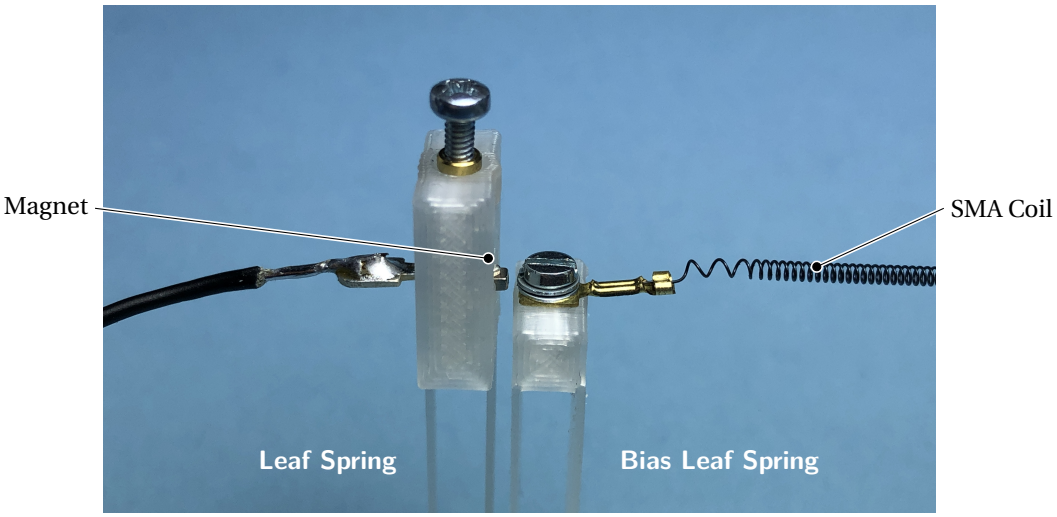

Figure 5.4: The close-up structure of the magnetic latch system that acts as the oscillating electrical contact for the SMA coil. Here, the biasing leaf spring also act as a linear stage for the actuator.

time required to re-establish the electrical contact across the SMA depends on the cooling time of the SMA wire or coil. In the case where the SMA is cooled using passive thermal exchange with the surrounding air, the fall time can be controlled by adequately sizing the diameter of the SMA wire or coil. The amplitude of the system, in this case, depends on the latch system and can be sized using the equation 5.1. Furthermore, the stroke of the SMA actuator can be sized using the methods presented in chapter 3 so as to ensure that the actuator is capable of deforming to the levels demanded by the oscillator amplitude. This will ensure that the snap-through of the oscillator occurs before the SMA overheats.

The fall time of the control system can be calculated using a simple thermal model based on the passive cooling of the SMA wire or coil. Here, the time constant, τ_c, of the system in which the thermal exchange of heat from the surface of the SMA to the surround air is used to cool down the SMA can be expressed as :

$$\tau_c = \rho c d/(kH) \tag{5.2}$$

where ρ [kg/m^3] is the density, c [J/(kgK)] is the specific heat capacity, d is the wire diameter, $k = 4$ is the ratio between the surface area of heat exchange, A_S and the volume of the active element, V, and H [W/(m^{2}K)] is the heat transfer coefficient. The thermal model of the wire can be expressed as :

$$T(t) = T_R + (T_2 - T_R)e^{-t/\tau} \tag{5.3}$$

where T_R is the ambient room temperature and t is time. Thus, the cooling time, t_c, based on

the temperature gradient between the SMA and the surrounding air, can be expressed as :

$$t_c = \tau_c \log \frac{T_2 - T_R + \frac{T_2 - T_1}{2}}{T_2 - T_R - \frac{T_2 - T_1}{2}} \tag{5.4}$$

where the subscripts, 1 and 2, represents the operating points of the actuator as shown in chapter 3. The physical properties of the SMA were obtained by consulting the data given by the supplier at *Dynalloy*.

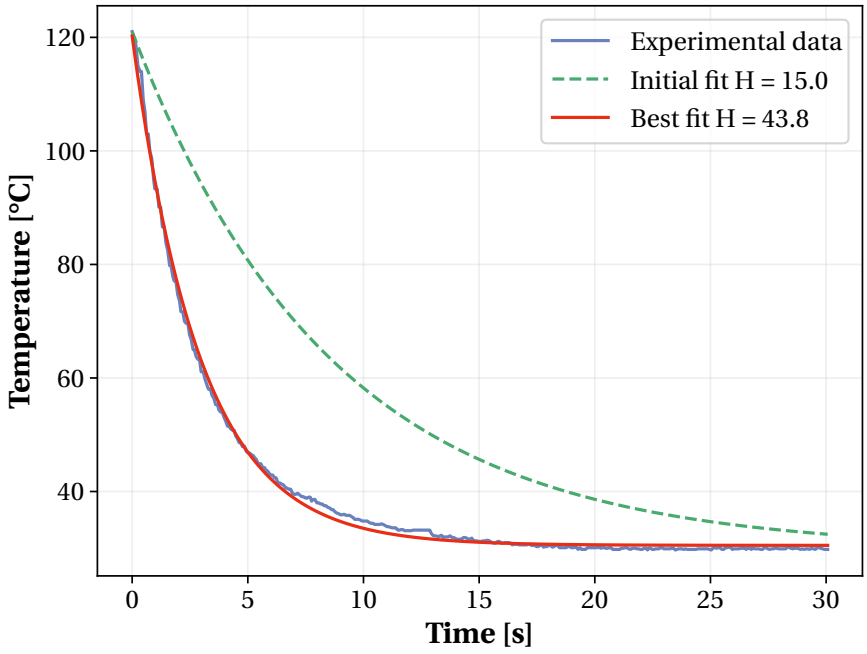

Figure 5.5: Measurement of the heat transfer coefficient, H, using 250 μm wire diameter SMA spring with a mandrel size of 0.5 mm.

Using a thermal camera with an optical zoom that allows for high spatial resolution and using equation 5.3, least-squares minimization is used to fit this thermal model to the cooling time of an SMA coil of 250 μm wire diameter. By doing so, the heat transfer coefficient, H, can be estimated. Using the model and the estimated parameters, the time constant and cooling times of other diameter SMA springs can be extrapolated. By extrapolating the cooling times of different diameter SMA springs, these values can be used to size this oscillator control system for other applications. In fig. 5.6, the cooling based on wire diameter of different SMA springs can be seen. Using these values, the fall time of the oscillator can be estimated for any wire diameter.

The rise time of the oscillator, t_h, can be estimated by calculating the time required to heat the SMA wire using Joule heating. Using the known resistance of the SMA wire, R, and the current, I, supplied to the system the heating time can be easily measured using the basic laws of electro-thermodynamics. In the case of slower rise time with small currents, the loss of

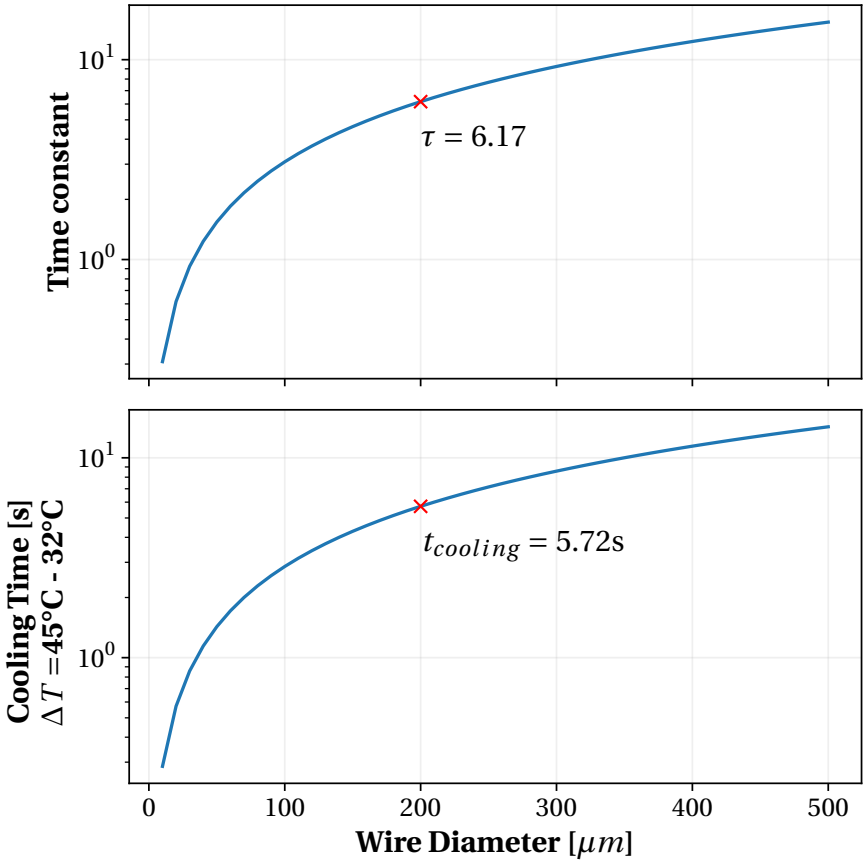

Figure 5.6: Extrapolation of the cooling time based on wire diameter with $H = 43.8$ W/(m^{2}K).

heat with the surrounding air by convection must be taken into account and can be estimated with the equation :

$$t_h = \int_{T_1}^{T_2} \frac{\rho V c}{I^2 R(T) - H A_S (T - T_R)} dT \tag{5.5}$$

The control system was supplied with a constant current and left to oscillate for 2 minutes to test the repeatability and consistency of the rise and fall times. The temperature of the SMA coil was measured using a thermal camera with high spatial resolution and the stroke of the SMA actuator was measured using a laser displacement sensor. In fig. 5.7, the temperature and position fluctuations of the oscillator are shown. The rise time of the magnetic latch-based control system when supplied with 340 mA was measured to be 3.8 ± 0.18 s while the rise time when supplied with 840 mA was measured to be 0.64 ± 0.09 s. The cooling time when supplied with 340 mA and 840 mA was found to be 5.71 ± 0.09 s and 5.82 ± 0.2 s, respectively. Thus, the period of the oscillations for the two measurements were found to be 9.60 ± 0.17 s and 6.47 ± 0.22 s which corresponds to a frequency of 0.10 Hz and 0.16 Hz.

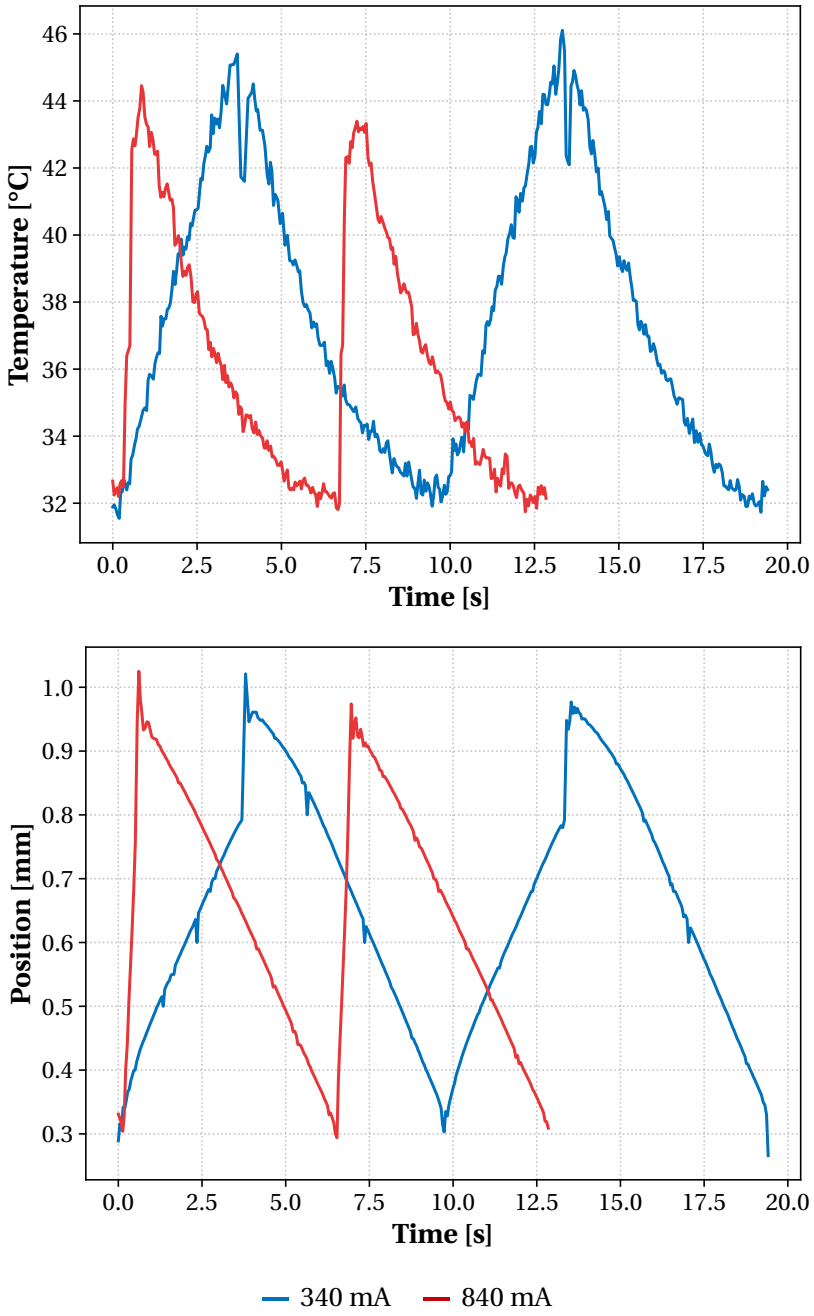

Figure 5.7: Effect of the current on the evolution of the SMA spring's temperature and position.

The rise time and cooling times of the latch-based control system were measured by detecting the peaks and troughs of the measured signals. The mean and standard deviation of these values were then calculated. Furthermore, the cooling time predicted, in fig. 5.6, based on the SMA geometry corresponds to the measured values, thus, validating the thermal model. Also, the cooling time remains relatively constant with respect to the varying current across the SMA. The cooling times can, thus, be predicted using the analytical model and the value

remains constant, even while varying the current. This implies that the control system can be sized for a fixed fall time by appropriately sizing the SMA wire diameter.

This magnetic latch system allowed the bias-spring SMA actuator to be actuated without any sensors or risk of overheating the SMA. The latch was required to allow the SMA to be heated during the entire stroke of the latch. A system using pogo pins, which are electric contacts consisting of a plunger and a spring mounted inside a barrel, was also tested. This resulted in a behaviour where the bias-spring SMA actuator oscillated at the tip of the pin. This, unfortunately, showcased the need for a latch system to bring the electric contact back to the starting position such that the actuator can carry out its entire stroke during the cooling phase. A latch system based on friction and snap-fits can be designed as an alternative. This pogo pin solution had the unexpected effect of allowing the SMA coil to be maintained at a stable temperature. This effect could be potentially used to stabilise an SMA at a fixed temperature based on the stroke of the pogo pin. The behaviour was not further explored in this paper.

5.3 Validation of the Approach using a Case Study

As stated previously, the requirement of sensors and complex control strategies in certain applications were compactness and being lightweight are required, pollute the overall work-weight density of the robotic system. In this section, to validate the novel design methodology for mechanical control solutions, a lightweight and compact crawling robot powered by shape memory alloys is designed and fabricated. Here, in the creation of an untethered crawling robot, the presence of sensors or micro-controllers will play an important role in the final work density of the system.

In this SMA driven crawling robot, the magnetic latch-based control system is implemented so as to create a small scale robot that can be driven without any sensors or electronics. In this mechanism, the high work density of the SMA is not compromised due to the lack of large biasing-springs and control electronics when compared to examples such as the work by cite.

5.3.1 Background and Biological Analysis

The mobile robot fabricated using this design approach is inspired by the gait of the inchworm. This insect is not a type of worm but in-fact, a type of caterpillar. These inchworms are known for their peculiar type of locomotion made possible by a looping motion called the two-anchor crawling gait, as described in the work by cite. Its gait consists of attaching its forelegs and using the muscles located in its abdomen to pull the rest of its body, as demonstrated in cite.

The gait, as seen in cite, consists of alternating between gripping or slipping against the ground. Initially, the forelegs are made to slip while the abdominal muscles push against the hing-legs which are now planted firmly on the ground. Nest, the forelegs are made to grip the ground and the abdominal muscles pull the rest of the body while the hind-legs slide across

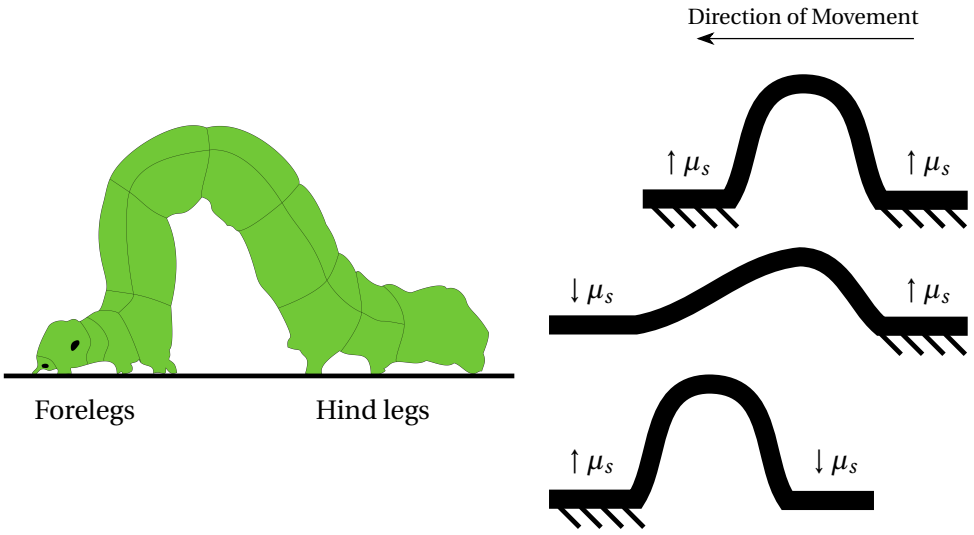

Figure 5.8: The gait analysis of an inchworm showing the insect change the coefficient of friction (μ_s) with respect to the ground by either gripping or sliding its legs.

the ground. This pattern is repeating to allow the inchworm to crawl across the surface. The presented mobile robot exploits this gait to create a similar crawling locomotion.

5.3.2 Working principle and Implementation of the Robot

The basic working principle of this mobile robots consists of implementing the design methodology presented in chapter 3 and the magnetic latch-based control system. Here, the linear movement of the SMA oscillator is transformed into a rotation of a pair of legs such that the tips or claws of the leg pulls the body of the insect robot across the ground.

As seen in fig. 5.9, the inchworm robot is entirely 3D printed in a single piece and is powered using an SMA coil. The control system used in this design is based on the approach detailed in section 5.2.2. The legs of the insect robot is attached to the end-effector of the SMA actuator so as to harness the strain recovery when the SMA coil is heated using Joule's heating. Here, as detailed in chapter 3, the biasing element of the SMA actuator consists of a flexure-based cantilever leaf spring. This biasing element also acts as a simple kinematic stage that transforms the SMA linear strain recovery into a rotation of the robot legs.

The insect robot operates in a similar manner to the inchworm presented in section 5.3.1 where the claws alternate between high friction and low friction with respect to the ground. By activating its artificial abdominal muscle consisting of the SMA coil, the insect robot is able to crawl across the ground. Here, the alternating friction that occurs at the claws is due to the design of the tips of the insect legs. The angle of the legs as the robot moves changes the angle of contact with the ground surface. As the leg tip design is asymmetrical with the direction of movement, the rotation of the legs cause alternating high and low friction. The behaviour is similar to a ratchet system where one degree of freedom is allowed in the forward direction but

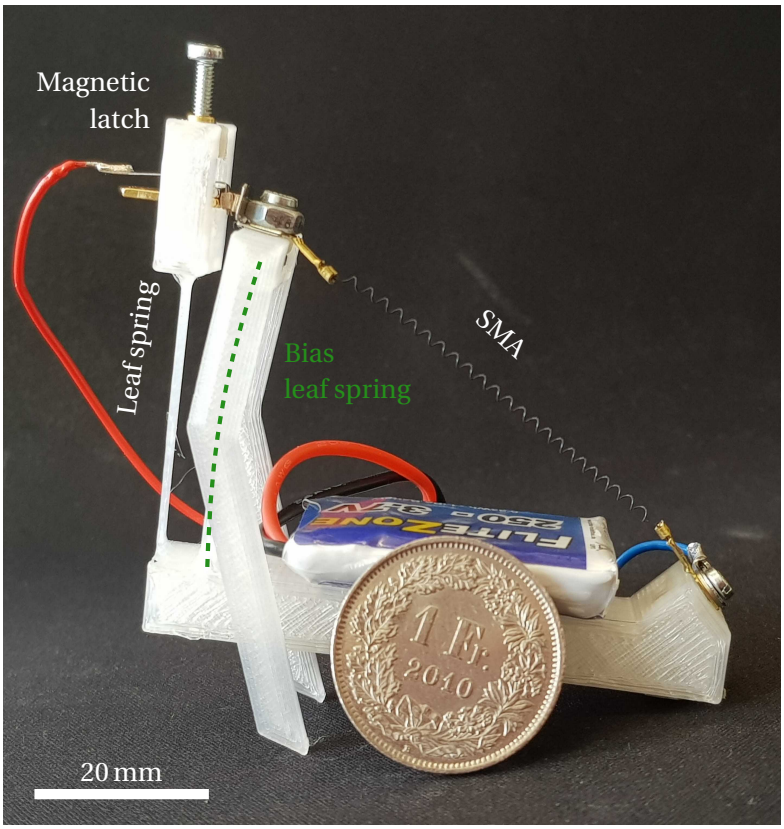

Figure 5.9: The implementation of the insect robot around the mechanical SMA oscillator.

not in the backward direction. Here, the claw design allows rotation in the clockwise direction but prevents some rotation in the anti-clockwise direction. As the SMA is heated, the insect robot moves its forelegs away from the body. Then, when the SMA coil is stretch by the biasing leaf spring during cooling, the forelegs grip the ground and drags the rest of the body along the ground. By repeatedly heating and cooling the SMA, the insect robot can gradually move across the ground. As detailed in this novel control strategy, the magnetic latch system allows the SMA to oscillate and control the steps of the insect robot without any micro-controllers or electronics.

5.3.3 Analytical model of the Biasing Compliant Mechanism

When sizing the design and SMA of the insect robot, an analytical model of the compliant mechanism is required. This models allows dimensioning the SMA coil such that sufficient stroke is observed during the shape memory effect. Here, the stroke of the SMA actuator or the contraction of the SMA coil corresponds to the estimated step length of the insect robot.

The crux of the design revolves around the flexure-based biasing element and kinematic stage which, in this design, consists of a simple cantilever leaf spring. This flexural structure converts the linear contraction of the SMA coil into the rotation of the insect legs while also serving as

the bias spring for SMA actuator allowing the coil to be stretched during the cooling phase based on the design approach detailed in chapter 3.

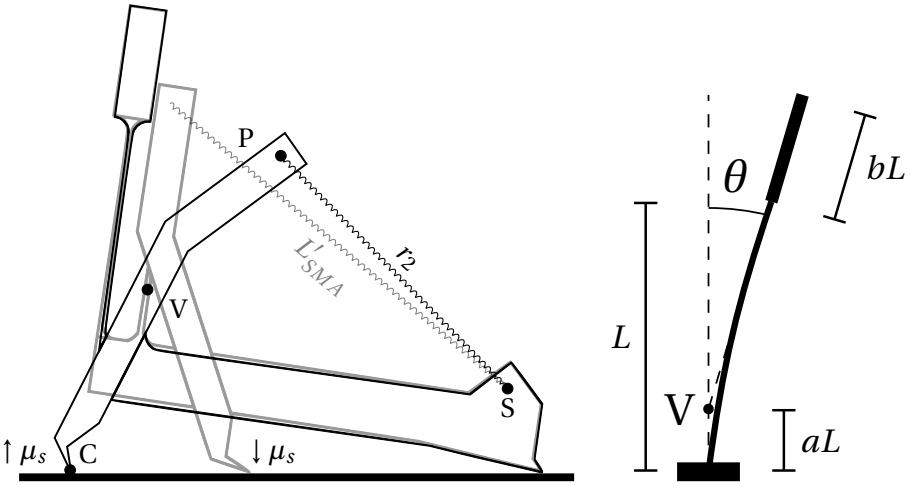

Figure 5.10: The working principle of the insect robot showing the simplification of the cantilever beam to a virtual rigid body pivot. The claw design changes the coefficient of friction (μ_s) of the insect with respect to the ground allowing the robot to crawl.

The pseudo-rigid-body model, as described in the work by Howell et al. (2013), is used to model flexure-based mechanisms such as the cantilever beam as traditional rigid-body mechanisms. Thus, by simplifying the cantilever leaf spring as a virtual pivot, an analytical model can be established to estimate the effect of the SMA coil contraction. In the work by Zhang et al. (2007), the location of the virtual pivot can be estimated with relative accuracy to a point at a distance of aL from the clamped end of the cantilever beam, where L is the length of the beam, bL is the length of the rigid attachment point with the SMA coil and a is:

$$a = \frac{1+3b}{3+6b} \tag{5.6}$$

The pre-stretched SMA coil of length, L'_{SMA}, is attached to the biasing cantilever leaf spring at the free end as shown in fig. 5.10. The position of cantilever tip, $P(x_P, y_P)$, as the SMA coil contracts in length by ε, can be deduced by finding the intersection between the two circles with radii, r_1 and r_2, and with centres at the virtual pivot $V(x_V, y_V)$ and fixed end of the SMA coil $S(x_S, y_S)$, respectively.

$$P(x,y) = \frac{1}{2}\begin{pmatrix} x_V + x_S \\ y_V + y_S \end{pmatrix} + \frac{r_1^2 - r_2^2}{2R^2}\begin{pmatrix} x_S - x_V \\ y_S - y_V \end{pmatrix} \pm \frac{1}{2}\sqrt{2\frac{r_1^2 + r_2^2}{R^2} - \frac{(r_1^2 - r_2^2)^2}{R^4} - 1}\begin{pmatrix} y_S - y_V \\ x_V - x_S \end{pmatrix} \tag{5.7}$$

where R is the Euclidean distance, $|\overline{VS}|$, between the two circle centres, $r_1 = (1 - a + b)L$ and

$r_2 = L'_{SMA} - \varepsilon$ representing the current length of the SMA coil.

As the insect legs are attached at the cantilever tip, the claw tips, $C(x_C, y_C)$, of the insect robot can be estimated by using a series of simple translation and rotation transformations from the cantilever tip based on the angles (α) and lengths (L) of the insect leg segments.

$$C(x,y) = \begin{pmatrix} x_P \\ y_P \end{pmatrix} + \sum_{i=1} L_i \begin{pmatrix} \cos(-\frac{\pi}{2} - \theta + \sum_{i=1} \alpha_i) \\ \sin(-\frac{\pi}{2} - \theta + \sum_{i=1} \alpha_i) \end{pmatrix} \tag{5.8}$$

Thus, based on the contraction or strain recovery of the SMA coil (ε), the step length of the insect, ΔC, can be estimated by taking the Euclidean distance between the claw tip location before and after the SMA contraction. The position of the insect robot claw and the step length based on the SMA coil contraction can be seen in fig. 5.11.

5.3.4 Implications of the Prototype

As detailed in the methodology, the analytical model of the inchworm robot that determines the relationship between the contraction of the SMA during actuation and the estimated step length was first estimated. This design was simulated using a commercial finite element modelling (FEM) software which was then used to validate the analytical model, as shown in fig. 5.11. Furthermore, the experimental results obtained from the inchworm prototype was used to validate the model, as shown in the same figure. This comparison shows that the pseudo-rigid body model used to model the design is quite accurate and can thus be used to further optimize the step length in future iterations.

Table 5.1: The design parameters of the inchworm robot.

Parameter	Value
SMA dimensions	Coil: ∅1.37 × 12 mm Wire: ∅0.2 mm
Biasing Leaf Spring	30 × 10 × 0.6 mm
Magnet Leaf Spring	30 × 2.5 × 0.6 mm
Magnet force	250 g
Battery Life	1.6 min @ 20 mAh

Due to the design being based on flexure-based structure, the inchworm could be fabricated from a single 3D printed piece. The structure was printed from PLA filament using fused deposition fabrication based on the parameters shown in table 5.1. Due to the novel control system based on the magnetic latch, when connecting the robot to a 20 mAh battery, the robot

is able to crawl untethered , as shown in fig. 5.12, for an estimated 1.6 min. When allowed to crawl on a flat surface, the average speed of the insect robot was measured to be 1.55 mms^{-1}, as shown in fig. 5.13. The efficiency of the leg design is highly dependant on the surface; smoother surfaces cause the legs to slip and drastically changes the overall efficiency of the design.

As stated, the principle advantage to the novel control system approach is the absence of sensors or micro-controllers. Using this methodology, the total weight of the robot including the battery weights 9.7 g. The insect robot is powered using only a single SMA coil. As with most SMA actuators, the coil is heated using Joule's heating by passing a current through it. Here, the heating consists of passing a 770 mA current for a duration of 750 ms with a power of 1.7 W. As shown in fig. 5.11, the step length of the insect robot was measured to be 8 mm.

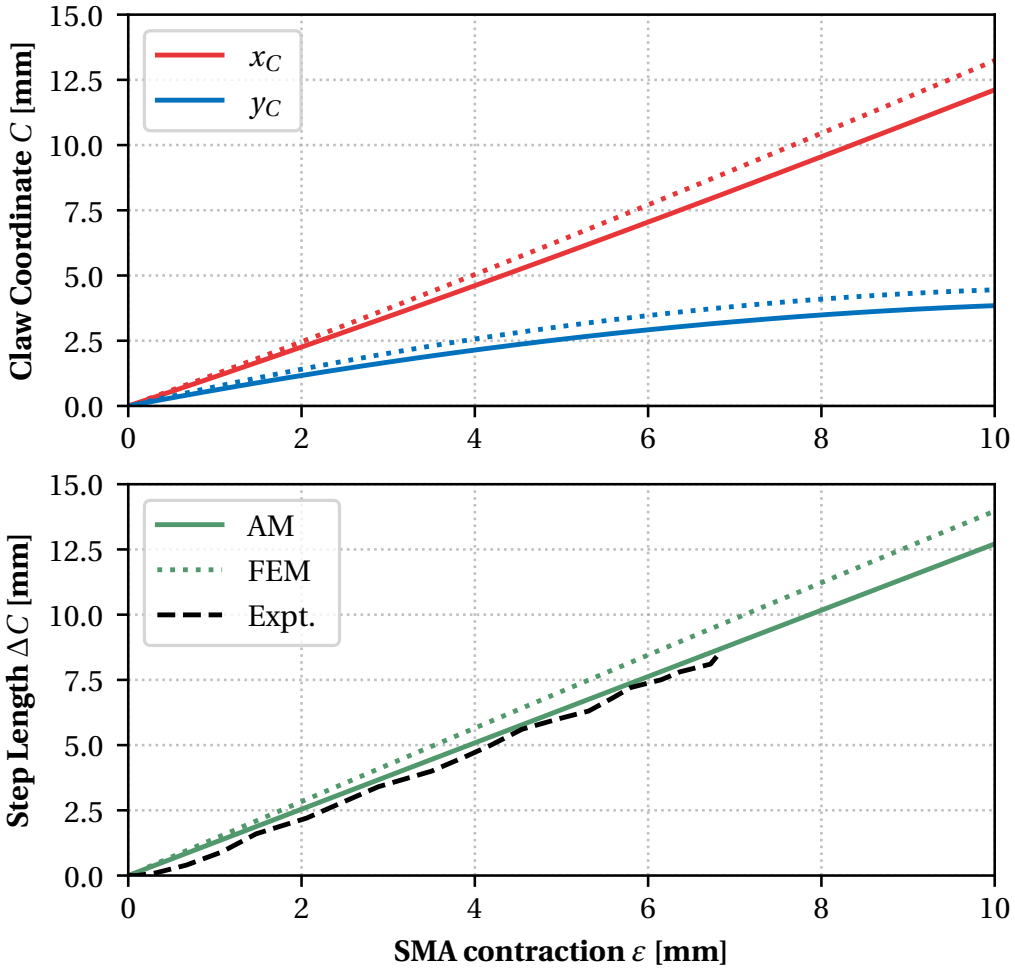

Figure 5.11: Comparison of the leg tip displacement versus the contraction of the SMA coil between the analytical model (AM) and Finite Element Model (FEM) simulation. Here, the dotted and filled lines represent the FEM results and analytical model, respectively.

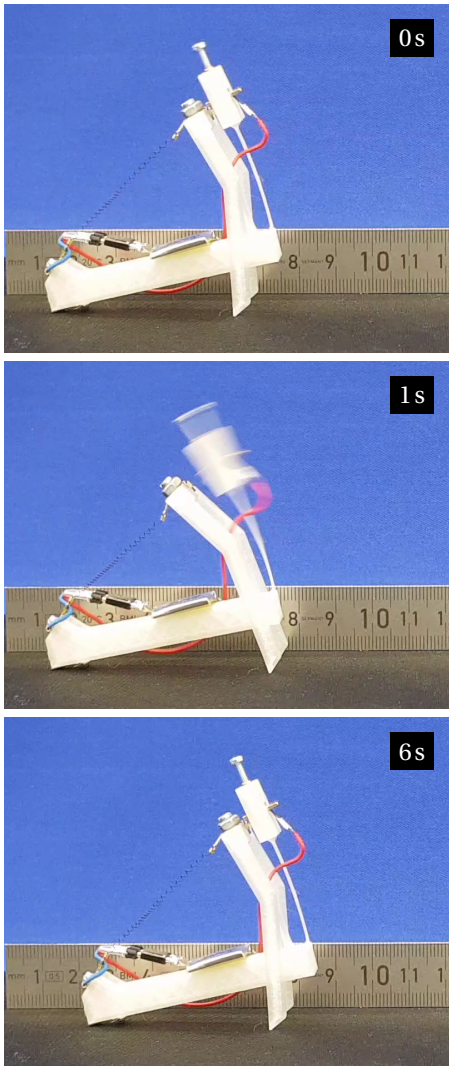

Figure 5.12: The untethered gait of the insect robot with a step length of 8.4 mm. As predicted, the snap-through of the magnetic latch halts the heating of the SMA coil.

Often, in the case of mobile robots, especially bio-inspired robots, the cost of transport (CoT) is calculated to compare the design and implementation. This factor allows the comparison of mobile robots with varying structures, sizes and gaits. It can be calculated using the following equation :

$$\text{CoT} = \frac{E}{mgd} \tag{5.9}$$

where E is the energy required to heat the SMA, m is the total mass of the robot including the battery, g is the acceleration due to gravity and d is the step length of the robot. Using the equation, the CoT was calculated to be around 1620 $\text{Jkg}^{-1}\text{m}^{-1}$. This is comparable to other untethered inchworm robots like in the work by Ji et al. (2019) whose CoT is measured to be 1670 $\text{Jkg}^{-1}\text{m}^{-1}$. However, when compared to other inchworm robots, as shown in table 5.2,

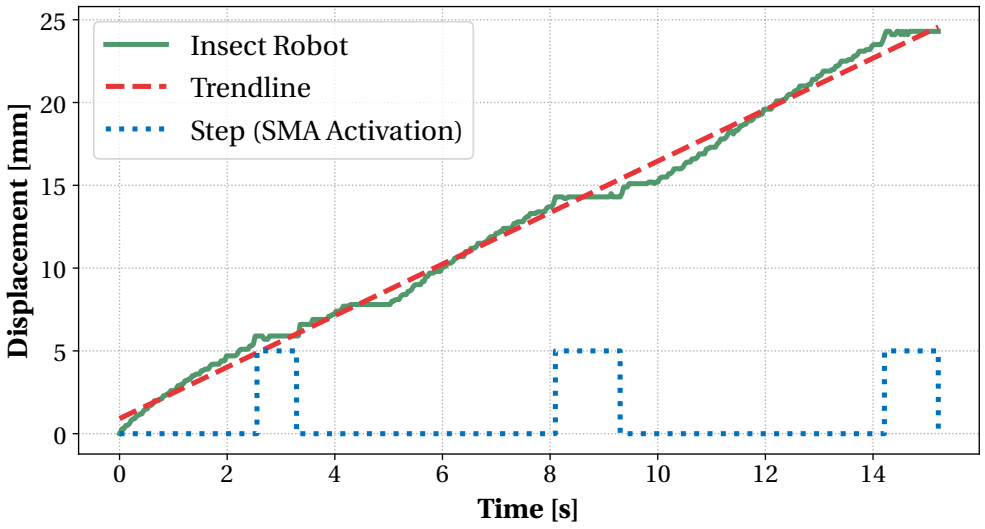

Figure 5.13: The displacement of the insect robot. The average speed of the robot is 1.55 mms^{-1}. Here, the step line represents the state of the SMA. A high value denotes that the SMA coil is being heated and a low state denotes that the SMA coil is cooling down.

this work is limited in the overall speed. This can be explained due to the inefficiency in the claw design and the dependence on the friction with the ground. The design, while being cheap and easily fabricated using 3D printing, it is limited by the PLA material. By optimizing the material to create thinner leaf springs, the size of the robot can be greatly reduced. Future work will have to include the optimization of the claw design and improve the overall efficiency of the insect robot's claw design to prevent slipping.

5.4 Summary and Conclusion

In this chapter, a novel approach to design a mechanical control system is presented. In this methodology, the control stage of a traditional SMA actuator is integrated into the kinematic stage of the actuator. This results in a control mechanism that uses the thermomechanical behaviour of the SMA such that the system no longer requires any sensors or electronics.

Furthermore, a basic implementation of such a system is presented using a magnetic latch-based system. Using a magnet and flexure-based cantilever leaf springs, a magnetic latch was designed and implemented where after a certain stroke threshold, results in an instantaneous snap-through. This rapid bifurcation is exploited to instantly disconnect mechanically the electrical contact across the SMA and thus, preventing any overheating. This design principle was implemented by fabricating a basic SMA mechanical oscillator that requires no sensors or electronics to oscillate.

Lastly, the design methodology was validated using a case study consisting of an untethered crawling insect robot powered by a single SMA coil. Here, based on the presented design

Table 5.2: Comparison of various different smart material based mobile robots using data from the work by Ji et al. (2019)

Smart Material Technology	Robot length (BL) [mm]	Speed [mms^{-1}]	Speed [BLs^{-1}]	Total weight [g]	Speed / weight [BLs^{-1} per g]
SMA [This work]	60	1.55	0.03	9.7	0.003
SMA [Koh and Cho (2013)]	150	10	0.07	1.2	0.055
SMA [Huang et al. (2018)]	57	34	0.6	~20	0.03
DEA [Ji et al. (2019)]	40	12	0.3	0.97	0.3
DEA [Cao et al. (2018)]	200	4	0.02	252.6	8×10^{-5}
Pneumatic actuator [Tolley et al. (2014)]	650	5	0.008	~4000	2×10^{-6}
IPMC [Must et al. (2015)]	45	0.45	0.01	0.83	0.01

methodology, a biasing flexure-based SMA actuator was modelled and sized to power the crawling robot. Furthermore, the control system presented in this chapter, was implement using the magnetic latch system so as to create a reversible control scheme for the SMA actuator. The kinematic stage, which acts as the biasing element of the SMA actuator, is exploited within the control system. Based on the results from the locomotion of the insect robot, a regular step size and walking speed is observed, thus, validating the design approach presenting in this chapter.

Using the methodology presented in this chapter, a novel control system can be designed and sized such that the SMA actuator can be controlled without the need for bulky sensors and micro-controllers and without the risk of overheating the SMA element.

6 Validation using Novel SMA Gripper Systems

6.1 Introduction

In this work, a design methodology is presented to design and size novel SMA actuators. By adapting the sizing methodology and design parameters of traditional SMA actuators, an approach is formed that can be exploited to create more compact and integrated solutions for actuators powered by shape memory alloys. In this final chapter, the novel design methodology is validated using different case studies. These case studies employ the strategies and analytical models presented in the previous chapters to adequately size compact and lightweight grippers. While validating the different analytical models, these case studies also validate the basic premise of the methodology.

The primary advantage of SMAs being their relatively high energy work density when compared to smart materials, they can be exploited to create powerful actuators for applications where low weight and compactness are required. In this context, a common application for SMAs are in actuators used to power grippers for drones or pick and place machine as shown in the work by citeand cite. Here, primary criteria to take into account are the overall dimensions, weight and time responses of the gripper. Using the design methodology presented earlier, the force and stroke requirements of the application can be taken in account such that the sizing of the SMA actuator can result in a gripper that is still integrated and fast.

6.2 Case Study: A Multi-Output SMA Mandrel

6.2.1 Motivation and Background

As previously stated, Shape Memory Alloys exhibit a relatively high volumetric work density. Thus, they are an ideal candidate in created lightweight actuators for applications where reducing the total weight of the system drastically improves the efficiency such as drone deliveries. Here, any reduced weight increases the total flight time of the drone and thus, makes it the ideal use case of lightweight SMA actuators. In the context of drone deliveries, grippers

generally consist of an actuator such as a motor and kinematic stage that converts the motion of the actuator into a gripping motion. In certain scenarios, the required gripping motion can be complex consisting of multiple outputs and radial movements such as gripper implemented in cite(iris gripper). In this case study, the goal is to apply the design methodology presented in chapter 3 to fabricate a drone-ready gripper with an advanced gripping mechanism. Using compliant mechanisms generated by topology optimization, an advanced kinematic stage can be designed to convert the motion of the SMA actuator into a multi-output gripping motion. Based on the design approach, the multi-output SMA gripper is sized and fabricated so as to validate the methodology.

6.2.2 Working principle

The working principle of the proposed SMA gripper is based on the traditional SMA actuator presented in chapter 1 adapted by the design methodology described in chapter 3. Here, the gripper consists of a simple SMA coil that acts as the active element and an accompanying compliant structure that behaves as the kinematic stage and as the biasing element.

The active SMA coil is prestretched by the biasing element at low temperature and contracts when heated above its transition temperature. The biasing element, which also acts as a conversion mechanism to transform the linear actuation of the SMA coil into a gripper movement, exhibits an inherent stiffness due to the fact that it composed of flexure-based hinges. As the SMA cools down, a spring force acts on the coil due to the stiffness of the compliant mechanism. When heating the SMA, the contraction of the coil deforms the compliant biasing element creating the desired gripping motion at the output. By controlling the temperature of the SMA coil, the entire system can be made to grip and release objects.

In this application, the SMA coil is heating using Joule's heating by applying a constant voltage across it. This simple solution makes use of the internal resistance of the SMA coil to exploit the Joule's losses when passing a current through it to raise the temperature of the material. The coil, here, is cooled using passive cooling by simple convection with the surrounding air. This standard solution allows for a simple control system that does not require any external heating system which would add weight to the system. Furthermore, an H-bridge is used to supply the current and control the heating of the SMA coil. Finally, as precise control of the system is required, a hall-effect sensor or any other low profile position sensor can be used to detect the state of the gripper.

The working principle can be further visualised using the simplified sizing graphs presented in section 3.4.1 as shown in cite. The SMA coil within the gripper operates between the ambient temperature and a temperature above its transition temperature. This behaviour, as mentioned previously, can be simplified into two straight lines based on its temperature. It is important to note that there exists a locus of lines representing the SMA at every temperature in between. Based on the methodology, the operating point of the gripper can be deduced using the intersection of the SMA curves and the characteristic of the designed biasing element.

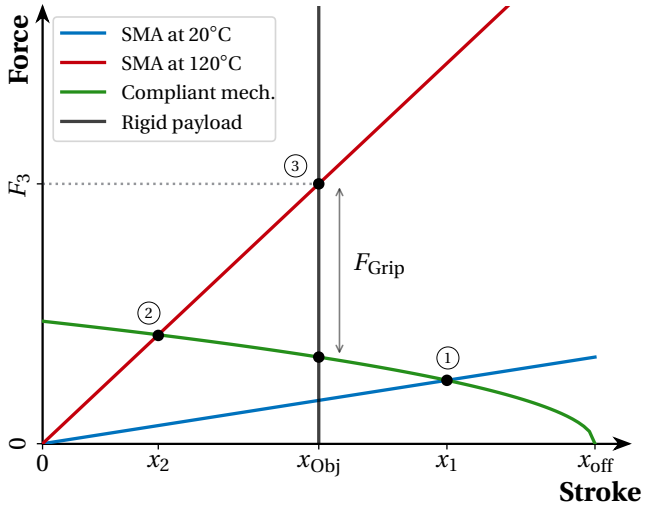

Figure 6.1: The working principle of the multi-output gripper based on the proposed designing methodology.

This characteristic will be described and validated in the following sections. The operating points are labelled in the figure as ① and ②. The maximum possible stroke of the gripper can be estimated by taking the difference between the x-values of the two operating points, $x_1 - x_2$. However, the variable, x_{off}, represents the distance between the SMA and the biasing-element before they are prestretched and attached to each other. These operating points described represent the behaviour of the gripper without a payload. In the case a payload, is present, the behaviour of the gripper and the gripping force is dependant on the size of the payload, x_{Obj}. This behaviour of the payload can be simplified as a perfectly rigid object with an infinite stiffness. Thus, the intersection between the force-displacement curve of the payload and the high temperature SMA will deduce the last operating point ③. The gripping force, F_{Grip}, experienced by the payload can be estimated using this last operating point as shown in the figure. Thus, as established by the design methodology presented in chapter 3, the curves of the SMA and the compliant mechanism can be used to estimate the total stroke and gripper force of the system.

6.2.3 Designing the Integrated Biased Kinematic Stage

The main goal of the design presented in this section is to create a multi-output gripper actuated using a single SMA coil. When designing grippers with complex outputs such as the work shown in cite, multiple active elements are used. The goal of this design is to improve these grippers by implementing an integrated system that can present multi-output gripping motion while only using a single SMA coil as an input. Here, the design is based on the 4-Point Mandrel topology presented in chapter 4. As mentioned within the chapter, using the current fabrication technology, it is not cost effective to fabricate the structure from the shape memory alloy. In this gripper design, the 4-prong radial compliant mechanism is used as the

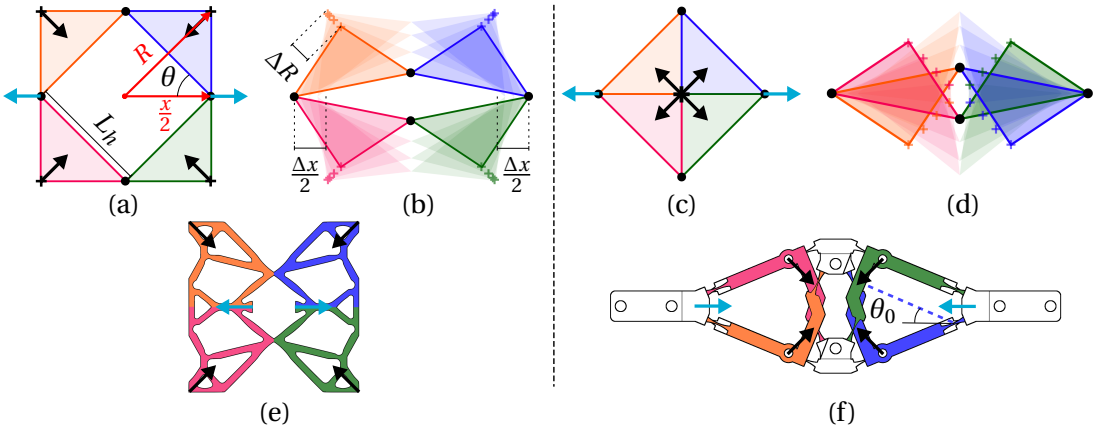

Figure 6.2: Kinematic diagram of proposed design where the black dots represent ideal pivots, the blue and black arrows represent the input and output displacement, respectively. On the left: the outward-triangle configuration with a) the initial position and b) the displaced one. On the right-hand side: the inward-triangle configuration achieving a stroke amplification with c) the initial position and d) the displaced one. e) represents mandrel topology generated with 2D topology optimization which behaves similarly to the outward version. f) shows the 2.5D adaptation of the inward version into a flexure-based mechanism distributed over multiple layers, and with a reversed actuation direction.

passive biasing element and as the kinematic stage. Furthermore, the compliant mechanism is redesigned using flexure-based hinges so as to improve the stroke of the gripper system. Here, as the topology is limited to the 2D plane, the flexural mechanism is further improved by extending the design space to a 2.5D design, which involved stacking 2D structures along the third dimension.

Articulated Parallelogram Core and Analytical Geometry Approach

The algorithmically generated mandrel topology consists of an articulated symmetrical parallelogram (rhombus). The topology can be reduced to four identical triangles joined at one vertex by a pivot as shown in fig. 6.2(a). The kinematics of the design is adapted from the generated one by using hinges instead of distributed deformation. In the figure, the blue arrows represent the input while the black arrows represent the output. The design has been generated such that the SMA coils can be placed at the inputs so as to generate a radial output towards the centre when actuated.

When examining the concept behind the mandrel mechanism, the conclusion can be made that the driving structure consists of four right-angled isosceles triangles which represent the four claws of the mandrel. Furthermore, the pivots, being constrained along the horizontal and vertical axes due to symmetry, force the outputs to move along a 45° path. However, upon careful examination, these constraints can be satisfied in two distinct configurations as shown in fig. 6.2(a) and (c). The four triangles can be position inwardly or outwardly. Due to the

inward-facing configuration having overlapping triangles, this topology cannot be generated from a 2D design space. The main advantage of the inward-facing configuration compared to the outward-facing configuration is the stroke amplification of the output vertices based on the stroke of the SMA coil contraction. It is also important to note that the direction of the radial output depends on the direction of the input displacement. Thus, the gripper can be made to open or close when the SMA coil is heated. By attaching the SMA coil to the vertical pivots rather than the horizontal ones, the gripper can be made to be always opened or always closed.

Determining the Relationship between the Hinges and the SMA Stroke

The stroke amplification, γ, of the system is not uniform and is dependant on the position of the mechanism, x. This amplification factor can be described by deriving the output vertex position, R, with respect to the input vertex position, x, and can be expressed analytically as :

$$\gamma(x) = \frac{\partial R(x)}{\partial x} = \frac{1}{2\sqrt{2}} \left(1 - \text{sign}(\alpha) \frac{x}{\sqrt{L_h^2 - \left(\frac{x}{2}\right)^2}} \right) \tag{6.1}$$

where,

$$\begin{aligned} R(x) &= L_h \cos\left(\theta(x) - \alpha\right) \\ &= \frac{1}{\sqrt{2}} \left(\frac{x}{2} + \text{sign}(\alpha) \sqrt{L_h^2 - \left(\frac{x}{2}\right)^2} \right), \end{aligned} \tag{6.2}$$

with,

$$\theta(x) = \arccos\left(\frac{x}{2L_h}\right) \quad \text{and} \quad \alpha = \pm\frac{\pi}{4}. \tag{6.3}$$

Here, L_h represents the length of the hypotenuse of each triangle, θ represents the angle between the horizontal and the hypotenuse, α represents the angle between the hypotenuse and the side of the triangle and can equal a value of $\pm\frac{\pi}{4}$. This angle is defined as positive for the outward-facing configuration and as negative for the inward-facing one. Here, the output stroke is majorly dependant on the sign of the angle α. The outward configuration has a stroke amplification of less than one for almost all possible inputs, implying a stroke reduction. While, on the other hand, the inward configuration has a stroke amplification large than one. In the context of a gripper, the inward version was chosen for its larger output stroke.

Simple Kinematics to a Compliant Mechanism

The kinematic schematic is composed of only simple hinges and rigid links. This makes it the ideal candidate for implementation using flexure-based hinges. In this case, as shown in fig. 6.3, truncated semi-circular flexure hinges were selected for their ability to avoid high localised stress concentration and allow for an acceptable angular stroke as displayed in the

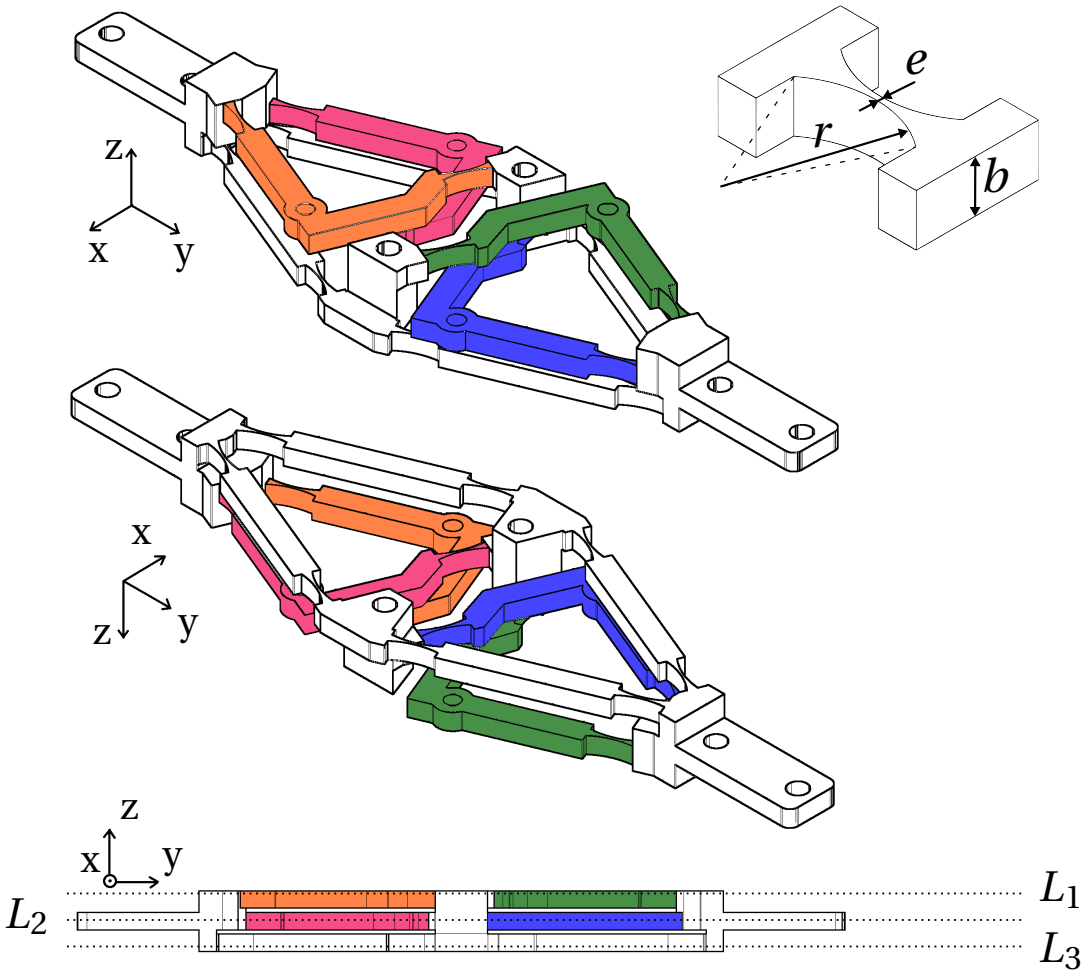

Figure 6.3: Different views of the flexure-based compliant mechanism spreading over multiple stages, and parametrized flexure pivot.

work by cite.

As stated earlier, the inward-facing triangle configuration was chosen and due to fact that the triangles overlap during actuation, it makes it impossible to be implemented in a 2D design space. Thus, as shown in fig. 6.3, a 2.D design approach was implemented where each overlapping triangle is stacked in the 3rd dimension. The mechanism is distributed among different superimposed layers linked at the vertices of the triangle to replicated the kinematic schematic. This adaptation to 2.5D design does not impact the functionality of the mechanism as long as the hinges are considered infinitely rigid when bending in any other direction other than the desired one. Here, two layers are implemented to accommodate the four triangles : the L_1 stage comprising of the green and orange triangles, and the L_2 stage comprising of the pink and blue triangles.

In the case of the ideal kinematic schematic, the triangles are attached at a single point to

form a parallelogram. However, this is difficult to implement with a flexure-based solution due to the rigid links having a non-null width. This adds unwanted links and hinges to the kinematic chain which results in undesired Degrees of Freedom (DoF). This parasitic DoF is overcome by adding a third DoF-inhibiting stage, L_3, to the 2.5D design as shown in fig. 6.3.

As the goal of this gripper is for drone delivery purposes, another stage, which behaves as the frame of the drone, can be added to the design. For mechanism to behave as intended in the kinematic schematic, the left and right input vertices must be constraint to move along a single line. In this case, for simplicity, this constraint has been implemented using a rail. For a future drone mounted setup, an additional stage can be added to perform this required constraint, showing the advantage of the 2.5D design approach.

Sizing of the Biasing Compliant Mechanism

Based on the proposed design methodology, the goal of the mechanism is to create a kinematic stage that also behaves as the passive biasing element for the SMA coil. The inherent stiffness of the overall compliant mechanism due to the flexural hinges is harness to prestretch the SMA for activation. Thus, in order to size the actuator and the corresponding biasing element, an analytical model of the stiffness must be developed. Using the pseudo-rigid model, as presented in the work by Henein (2005), the flexural hinges can be considered as torsional spring with a constant angular stiffness, K_θ. As detailed in chapter 3, the stiffness of the compliant structure requires an expression for the relationship between angular position of the flexural hinge and the contraction of the SMA, $\theta(\Delta x)$. In this case, this relationship can be expressed as :

$$\theta(\Delta x) = \arccos\left(\frac{\Delta x}{2L_h} + \cos(\theta_0)\right), \tag{6.4}$$

with θ_0 being the resting angle at which the mechanism is printer/fabricated as shown in fig. 6.2(f).

As detailed in the methodology, the next step is to calculate the potential energy within the system during deformation. Due to the symmetry of the mechanism, all the hinges store the same potential energy. Here, the L_3 stage has 8 hinges while the stages L_1 and L_2 have 4 hinges each. Thus, the total potential energy of the whole mechanism is :

$$U_{\text{tot}}(\Delta x) = 16 \cdot U(\Delta x) \tag{6.5}$$

The force-displacement characteristic of the mechanism is then given by :

$$\begin{aligned} F(\Delta x) &= \| -\nabla U_{\text{tot}}(\Delta x) \| = \frac{\partial U_{\text{tot}}(\Delta x)}{\partial \Delta x} \\ &= \frac{8K_\theta}{L_h} \frac{(\theta(\Delta x) - \theta_0)}{\sin(\theta(\Delta x))}. \end{aligned} \tag{6.6}$$

The resulting characteristic is plotted as shown in fig. 6.4. Furthermore, the model is validated

using experimental results obtained using a pull-tester. As the experimental results follow the model quite closely, it validates the working hypothesis and approximations used during the definition of the analytical model. As the force characteristic flattens unlike a traditional

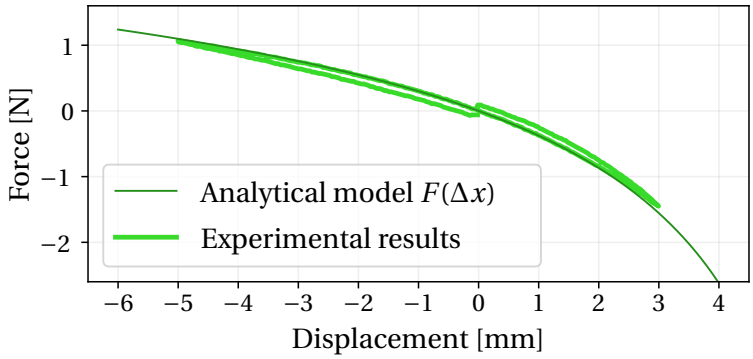

Figure 6.4: Validation of the analytical model of the biasing compliant mechanism using experimental results obtained using a pull-tester.

linear spring, the operating points of the actuator will offer higher strokes for a given SMA coil. Furthermore, as the curve also decreases in value near the low-temperature operating point ①, its implies that the gripper can exert higher gripping forces for objects with a larger diameter. This shows that the current force-displacement characteristic of the proposed compliant mechanism is well suited as a biasing element in an SMA actuator. Finally, in the figure, some plastic deformation can be observed as the mechanism was deformed beyond above its admissible range during the test. The flexural hinges exhibit a limited angular stroke which is one of the limitations of such a design. However, the maximal admissible angle before permanent plastic deformation can be estimated using the work by Henein (2005) as :

$$\Delta\theta_{\text{adm}} \cong \frac{3\pi\sigma_{\text{adm}}\sqrt{r}}{4E\sqrt{e}}, \tag{6.7}$$

which in this context can be expressed :

$$\begin{aligned} \Delta x_{\text{adm},+} &= 2L_h\left(\cos(\theta_0 + \Delta\theta_{\text{adm}}) - \cos(\theta_0)\right) \\ \Delta x_{\text{adm},-} &= 2L_h\left(\cos(\theta_0 - \Delta\theta_{\text{adm}}) - \cos(\theta_0)\right) \end{aligned} \tag{6.8}$$

If $\mathbb{X}_{\text{eq}} = \{x \mid x_2 \leqslant x \leqslant x_1\}$ is the set of possible operating points (see fig. 6.1) and $\mathbb{X}_{\text{el}} = \{x \mid x_{\text{off}} + \Delta x_{\text{adm},+} \leqslant x \leqslant x_{\text{off}} + \Delta x_{\text{adm},-}\}$ is the set of admissible positions for elastic deformation as portrayed in equation eq. (6.8) and fig. 6.1. Then, based on the design methodology presented in chapter 3, the set of feasible operating points for the actuator $\mathbb{X}_{\text{f}}$ is given by their intersection:

$$\mathbb{X}_{\text{f}} = \mathbb{X}_{\text{eq}} \cap \mathbb{X}_{\text{el}}. \tag{6.9}$$

One of the goals of the sizing methodology for the compliant mechanism is to maximise the output stroke while avoiding permanent deformation during operation. Thus, the com-

pliant mechanism must be sized such that $\mathbb{X}_{eq} \subseteq \mathbb{X}_{el}$. This eliminates the need for precise temperature and positional control of the SMA coil during activation to protect the flexural hinges.

In this case, the output stroke of the gripper can be maximised by maximising the size $\mathbb{X}_f$ or by having the operating points be located at positions where the curve of the stroke amplification is high (from eq. eq. (6.1)). A trade-off exists as displacing $\mathbb{X}_f$ for higher stroke amplification tends to reduce the overall size. Based on table 3.1, various additional trade-offs for the proposed mandrel can be observed as summarised in table 6.1.

Table 6.1: Additional trade-offs observed when sizing the flexural compliant mechanism actuated by a given SMA wire or coil. Here, S_{mech} and t_{mech} are the surface area and the thickness of the entire compliant mechanism, respectively.

Parameter	Effects
$\frac{e}{r} \uparrow$	$\Delta\theta_{adm} \downarrow \Rightarrow \mathbb{X}_{el} \downarrow$
$e \uparrow \mid \frac{e}{r}$ fixed	$S_{mech} \uparrow$
$b \uparrow$	$t_{mech} \uparrow$
$x_{off} \uparrow$	$\mathbb{X}_{eq} \uparrow$, $\mathbb{X}_{el}$ shifted away from $\mathbb{X}_{eq}$
$L_h \uparrow$	$F_{grip} \uparrow$, $S_{mech} \uparrow$
$\theta_0 \downarrow$	$\gamma(x) \uparrow$, $F_{grip} \downarrow$, $\mathbb{X}_{el} \downarrow$

$K_\theta \uparrow \Rightarrow \begin{cases} \mathbb{X}_{eq} \uparrow \\ F_{grip} \downarrow \end{cases}$

As seen in the table, an optimal solution can be estimated based on the design parameters. However, in the case of L_h ad b, increasing them will always result in an increased stroke while increasing the overall size of the mechanism. This shows that there exists a trade-off between the weight/size and the output stroke which will be critical to ascertain based on the gripper specifications.

6.2.4 Implementation and Experimental Results

One of the main advantages of this integrated design is the simplicity of fabrication and assembly. The entire compliant structure is printed from Nylon (PA 2200 Polyamide 12) using selective laser sintering (SLS) as shown in fig. 6.5. As the mechanism consists of stacked layers, the entire structure was printed as a single piece.

In this prototype, the design parameters used are $e = 0.5$ mm, $r = 15$ mm, $b = 4$ mm, $L_h = 42.4$ mm, $x_{off} = 27.5$ mm and $\theta_0 = \frac{\pi}{8}$. Here, a linear output stroke of up to 4 mm is observed for each claw. The gripper force, however, is dependant on the size of the gripped object. For an object of diameter close to x_1, the gripping force will be maximal. Using a pair of load cells attached to two opposing claws, the gripping force was measured. The load cells were placed at different distances from the claws to simulated objects of varying sizes. The results

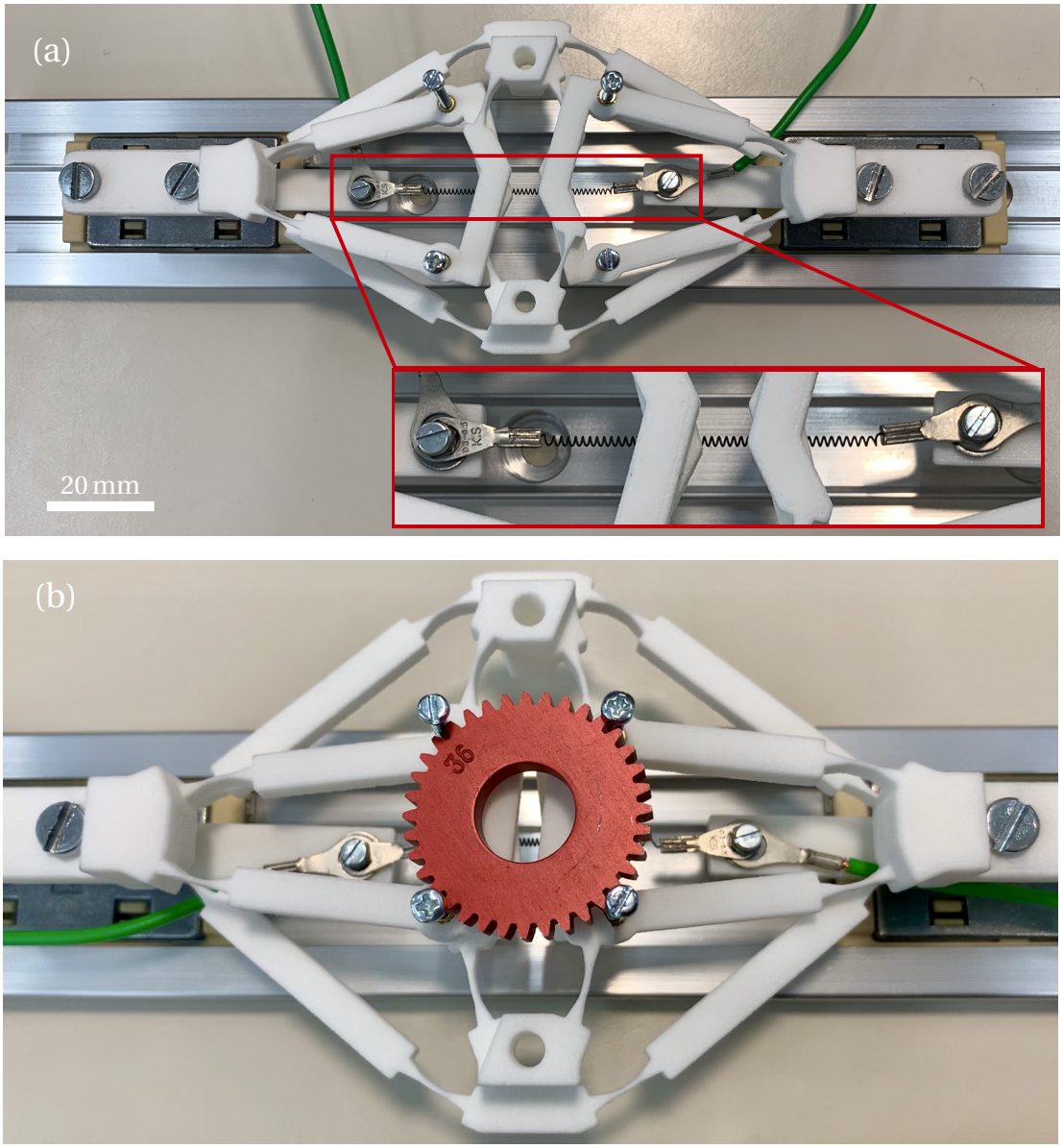

Figure 6.5: The working prototype of the biased-compliant SMA gripper (a) opened configuration with a 0.2mm wire diameter SMA coil (framed in red), (b) closed configuration grasping an object.

of the gripper force measurements can be seen in fig. 6.6. The gripper shows a force close to constant for large span of SMA temperatures above its transition temperature of 80°C . This constant force behaviour is ideal for a gripper and greatly simplifies the control, preventing any unintended damage to the gripped object. A maximum steady-state force of 1.78 N was measured for the biggest payload size while using the smallest available SMA coil, whose wire diameter is 0.2 mm. While this result is promising, it should be noted that the fabricated prototype is sub-optimal and can be further optimised for greater forces, either by optimising

the compliant mechanism or by using thicker SMA coils. Increasing the wire diameter of the SMA coil comes with higher gripping forces but comes at the cost of slower cooling time or increased time delay between the opening and closing sequence of the gripper.

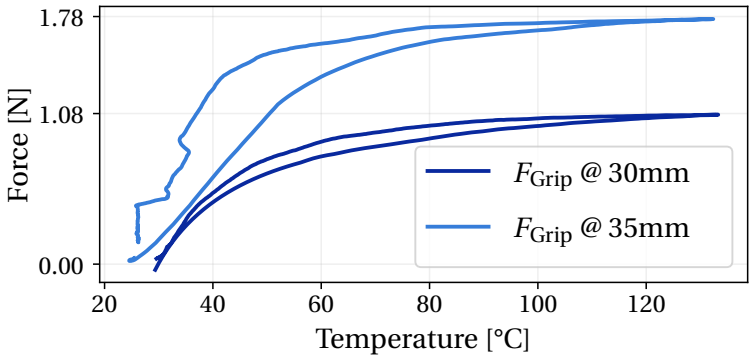

Figure 6.6: Results of the gripping force performed at different object diameters. The temperature and force output were recorded in real-time using a thermal imaging camera and a force sensor, respectively.

In the end, the final prototype, as seen in fig. 6.5, was measured to weigh only 17 g, which implies that the gripper has a maximum force-density of around 105 N/kg. This shows that proposed mandrel gripper can be ideal for lightweight applications such as drone deliveries. Furthermore, this demonstrates the highly integrated nature of the gripper, thus, validating the design methodology presented in chapter 3.

6.3 Case Study: A Bistable SMA Gripper

6.3.1 Motivation and Background

The core ideology behind SMA actuators has been to create miniature and compact systems that could potentially replace the current traditional solutions. In this work, the basic concept has been to discover methods by which the high energy dense nature of SMAs can be conserved when designing actuators.

This section has been motivated by the need to replace traditional pneumatic pick and place grippers that require large compressors to operate. These conventional pneumatic grippers, as they operate using compressed air and are a source of dust, are incompatible with clean-room applications. The primary motivation behind this section is to replace such a gripper and create a compact and lightweight solution that can be compatible with clean-room applications.

These pneumatic grippers are bistable grippers that fit within a small footprint with the disadvantage of requiring a wired connection to a large air compressor. Recently, SMAs have been paired with bistable elements to create actuator as shown in the work by cite. A simple but effective way to create a bistable element is to axially compress a beam such that they buckled. This buckled beam, which can be easily fabricated in varying dimensions, now can exist in two stable positions. The main advantage to using a bistable system is the fact that they require no additional energy to remain in these stable positions. They only require power when switching from one stable configuration to another. Thus, this behaviour can be further advantageous for designing grippers that often tend to remain in an open or closed position for extended periods of time such as drone-deliveries. As stated in previous examples, a fully compliant system can reduce the assembly complexity and weight while also preserving the life cycle if properly designed. Furthermore, a compliant bistable SMA-driven gripper can be the ideal candidate to replace the current pneumatic solution for clean-room pick and place applications.

6.3.2 Working Principle and Operation

In this design, the basic concept consists of combining antagonistic SMAs with a bistable compliant mechanism based on the proposed design methodology as described in section 3.4.2. Using a buckled beam, a simple bistable compliant mechanism can be designed such no energy is required to remain in the open or closed position of the gripper. As previously stated, the behaviour of SMAs are difficult to model accurately and predicting the shape memory effect can be quite difficult. Similarly, multistable mechanisms with snap-through behaviours are incredibly difficult to model mathematically and therefore, system pairing both SMAs and buckled beam are used but are, often, not adequately sized. Most work such as cite, present such a mechanism but lack the methodology to appropriately size the SMA. The SMAs used in such systems are often oversized and present with higher cooling times degrading the time

response and work density. However, in this work, using the proposed design methodology, the SMA buckled beam bistable gripper will be sized using the simplified models so as to create a gripper with reduced cooling times.

The basic principle of the presented gripper consists of using a pair of SMAs are external triggers to switch the buckled beam from one of its stable configurations to the other. In cite, a simple diagram of the system can be observed. Here, as mentioned, the buckled beam which is axially compressed exhibits the bistability and behaves as the compliant bistable mechanisms. The buckled beam is mounted at both ends using two supporting pivots and the snap-through is triggered by heating one of the two SMA coils. The initially straight beam, which can be fabricated as such, is buckled by bring together the support pivots. Here, one of the pivots is considered the input pivot and connected to the pair of SMA coils. The remaining pivot is considered the output and is connect to the jaws of the gripper.

The SMA coils, when heated, will contract and revert back to their original size. The input pivot is adapted to host a lever arm. As the SMA coils are allowed to contract, being attached to the lever arm, will cause the rotation of the input pivot. This rotation of the input pivot will, after a certain stroke, enable to rapid snap-through of the buckled beam switching it to its alternate stable position. Similarly, by heating the antagonistic SMA, the buckled beam can be made to switch back to its original stable position. Thus, by alternately heating either of the two SMAs, the compliant system can be made to switch back and forth between its two stable positions. As the SMA cools down, the complaint system requires no additional energy from the SMA coils to remain in the stable configurations and only requires energy when forcing the snap-through to occur.

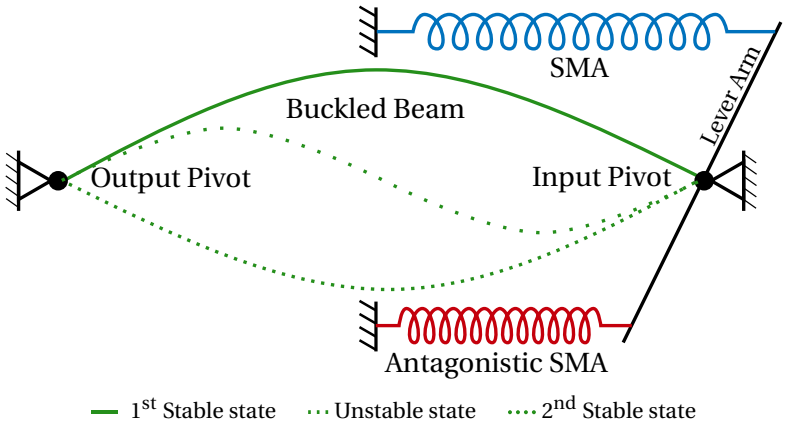

Figure 6.7: The schematic of the bistable SMA actuator composed on a buckled beam and a pair of SMA coils.

Compared to other bistable SMA actuators such as the work by cite, the real advantage of the proposed kinematic stage, using a buckled beam supported by pivots, is that gripping output is independent of the actuation input up to the point of snap-through. From the stable to unstable position of the buckled beam, the input lever makes a near full stroke while the

output pivot barely rotates. As soon as the unstable position is exceeded, rapid snap-through occurs and the output pivot switches instantaneously to the other stable stage, allowing for a rapid grasping or releasing motion.

6.3.3 Design of the Bistable Mechanism

The next step, as proposed by the design methodology, consists of defining the relationship between the contract of the SMA and the kinematic stage. In this section, the analytical model of the snap-through behaviour of the proposed bistable buckled beam is established. This model can then be used to design and size the buckled beam and the SMA coils so as to create a rapidly switching gripper with the required force and stroke specifications.

Analytical Model of the Buckled Beam

A beam theory model is proposed in this section to size the bistable buckled beam mechanism for the kinematic stage. In fig. 6.8, a schematic view of the buckled beam is shown. The initially flat beam buckled when compressed by a distance of Δl by the preloading stage attached to the input pivot. The SMA is considered to apply an input torque of M_{in} at the input pivot. As the final prototype of the kinematic stage is composed completely of flexure-based mechanisms, the pivots also present with an inherent angular stiffness, K_{in} and K_{out} at the input and output pivot, respectively. The buckled beam has flexural rigidity of EI and an initial length before compression of L. As the flexure-based pivots are not ideal, the extremities of the beam start at a distance of p from the centre of rotation of the pivots.

Based on the hypothesis described in the work by Tissot-Daguette et al. (2021) and the Euler-Bernoulli beam theory, the beam deflection can be expressed as :

$$y(x) = \left(A \sin kx + B(\cos kx - 1) + C\frac{x}{l} \right) l\theta_{\text{in}} \tag{6.10}$$

where $k = \sqrt{P/(EI)}$ and the boundary conditions are

$$y(0) = 0$$

$$y'(0) \cong \theta_{\text{out}}$$

$$M_0 \cong K_{\text{out}}\theta_{\text{out}} + Vp - Pp\theta_{\text{out}}$$

$$y(l) \cong -p(\theta_{\text{out}} + \theta_{\text{in}})$$

$$y'(l) \cong \theta_{\text{in}}$$

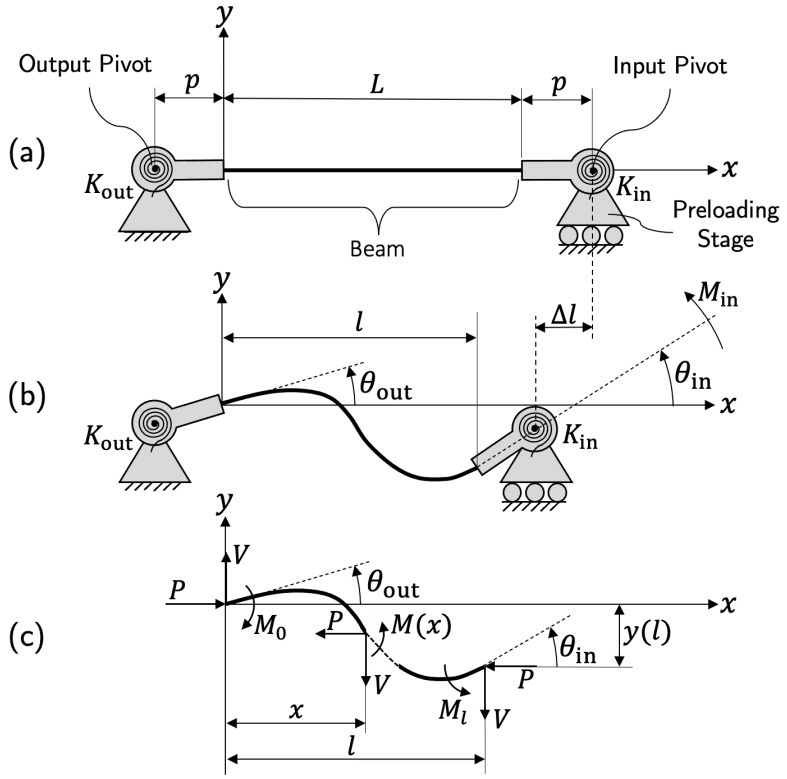

Figure 6.8: (a) As-fabricated, (b) deformed and (c) free-body diagram of the buckling beam.

Furthermore, the deflection parameters are given by

$$A = \frac{(1+2\overline{p})kl + \varepsilon_0\left(\overline{p}\sin kl - \frac{\cos kl - 1}{kl}\right)}{kl\left(kl\cos kl - \sin kl - \left(\overline{p}^2 + \overline{p}\right)(kl)^2\sin kl + \varepsilon_0\left(\sin kl + 2\frac{\cos kl - 1}{kl}\right)\right)} \tag{6.11}$$

$$B = \frac{\overline{p}(1+2\overline{p})(kl)^2 + \varepsilon_0\left(\overline{p}\left(\cos kl - 1\right) + \frac{\sin kl}{kl} - 1\right)}{kl\left(kl\cos kl - \sin kl - \left(\overline{p}^2 + \overline{p}\right)(kl)^2\sin kl + \varepsilon_0\left(\sin kl + 2\frac{\cos kl - 1}{kl}\right)\right)} \tag{6.12}$$

$$C = \frac{\overline{p}^2(kl)^2\sin kl - 2\overline{p}kl\cos kl - \sin kl - \varepsilon_0\left(\overline{p}\sin kl - \frac{\cos kl - 1}{kl}\right)}{kl\cos kl - \sin kl - \left(\overline{p}^2 + \overline{p}\right)(kl)^2\sin kl + \varepsilon_0\left(\sin kl + 2\frac{\cos kl - 1}{kl}\right)} \tag{6.13}$$

where $\overline{p} = p/l$ and $\varepsilon_0 = K_{out}/(EI/l)$. When considering the beam's arc length as constant, the end-shorting, Δl, can be approximated using the following expression

$$\Delta l \cong \frac{p}{2}(\theta_{in}^2 + \theta_{out}^2) + \int_0^l \frac{y'(x)^2}{2}dx = Hl\theta_{in}^2 \tag{6.14}$$

Here, the coefficient H is expressed as

$$H = \frac{\left(A^2+B^2\right)(kl)^2}{4} + \frac{\left(A^2-B^2\right)kl\sin 2kl}{8} + \frac{ABkl\left(\cos 2kl-1\right)}{4} + AC\sin kl + BC\left(\cos kl-1\right) + \frac{C^2}{2} + \frac{\overline{p}}{2}\left((Akl+C)^2+1\right) \quad (6.15)$$

By rearranging the eq. (6.14), the input angle is expressed as

$$\theta_{\text{in}} = \pm\sqrt{\frac{\Delta l}{l}}\sqrt{\frac{1}{H}} \quad (6.16)$$

Finally, the input moment can be described as the following eq. (6.17)

$$\begin{aligned} M_{\text{in}} &\cong M_l + K_{\text{in}}\theta_{\text{in}} + Vp - Pp\theta_{\text{in}} \\ &= \frac{EI}{l}\left((kl)^2\left(\overline{p}\left(C-1\right) - A\sin kl - B\cos kl\right) + \varepsilon_l\right)\theta_{\text{in}} \end{aligned} \quad (6.17)$$

where $\varepsilon_l = K_{\text{in}}/(EI/l)$.

6.3.4 Sizing of the SMA actuator

6.3.5 Integrated Control Strategy

6.4 Conclusion

Conclusion

A An appendix

Lorem ipsum dolor sit amet, consectetuer adipiscing elit. Ut purus elit, vestibulum ut, placerat ac, adipiscing vitae, felis. Curabitur dictum gravida mauris. Nam arcu libero, nonummy eget, consectetuer id, vulputate a, magna. Donec vehicula augue eu neque. Pellentesque habitant morbi tristique senectus et netus et malesuada fames ac turpis egestas. Mauris ut leo. Cras viverra metus rhoncus sem. Nulla et lectus vestibulum urna fringilla ultrices. Phasellus eu tellus sit amet tortor gravida placerat. Integer sapien est, iaculis in, pretium quis, viverra ac, nunc. Praesent eget sem vel leo ultrices bibendum. Aenean faucibus. Morbi dolor nulla, malesuada eu, pulvinar at, mollis ac, nulla. Curabitur auctor semper nulla. Donec varius orci eget risus. Duis nibh mi, congue eu, accumsan eleifend, sagittis quis, diam. Duis eget orci sit amet orci dignissim rutrum.

Bibliography

Alonso, C., Ansola, R., and Querin, O. M. (2014). Topology synthesis of Multi-Input–Multi-Output compliant mechanisms. *Advances in Engineering Software*, 76:125–132.

Andrianesis, K. and Tzes, A. (2015). Development and Control of a Multifunctional Prosthetic Hand with Shape Memory Alloy Actuators. *Journal of Intelligent & Robotic Systems*, 78(2):257–289.

Benard, W. L., Kahn, H., Heuer, A. H., and Huff, M. A. (1998). Thin-film shape-memory alloy actuated micropumps. *Journal of Microelectromechanical Systems*, 7(2):245–251.

Bendsoe, M. P. and Sigmund, O. (2013). *Topology Optimization: Theory, Methods, and Applications*. Springer Science & Business Media. Google-Books-ID: ZCjsCAAAQBAJ.

Cao, J., Qin, L., Liu, J., Ren, Q., Foo, C. C., Wang, H., Lee, H. P., and Zhu, J. (2018). Untethered soft robot capable of stable locomotion using soft electrostatic actuators. *Extreme Mechanics Letters*, 21:9–16.

Chouinard, P. and Plante, J. (2012). Bistable Antagonistic Dielectric Elastomer Actuators for Binary Robotics and Mechatronics. *IEEE/ASME Transactions on Mechatronics*, 17(5):857–865.

Haibin, Y., Cheng, K., Junfeng, L., and Guilin, Y. (2018). Modeling of grasping force for a soft robotic gripper with variable stiffness. *Mechanism and Machine Theory*, 128:254–274.

Henein, S. (2005). *Conception des structures articulées à guidages flexibles de haute précision*. PhD thesis, EPFL, Lausanne. Publisher: Lausanne, EPFL.

Henein, S., Bottinelli, S., and Clavel, R. (1998). Parallel spring stages with flexures of micrometric cross sections. In *Microrobotics and Microsystem Fabrication*, volume 3202, pages 209–220. International Society for Optics and Photonics.

Howell, L. L., Magleby, S. P., and Olsen, B. M., editors (2013). *Handbook of compliant mechanisms*. John Wiley & Sons, Inc, Chichester, West Sussex, United Kingdom ; Hoboken.

Huang, X., Kumar, K., Jawed, M. K., Nasab, A. M., Ye, Z., Shan, W., and Majidi, C. (2018). Chasing biomimetic locomotion speeds: Creating untethered soft robots with shape memory alloy actuators. *Science Robotics*, 3(25). Publisher: Science Robotics Section: Focus.

Ikuta, K. (1990). Micro/miniature shape memory alloy actuator. In *, IEEE International Conference on Robotics and Automation Proceedings*, pages 2156–2161 vol.3.

Ji, X., Liu, X., Cacucciolo, V., Imboden, M., Civet, Y., El Haitami, A., Cantin, S., Perriard, Y., and Shea, H. (2019). An autonomous untethered fast soft robotic insect driven by low-voltage dielectric elastomer actuators. *Science Robotics*, 4(37):eaaz6451.

Jin Qiu, Lang, J. H., and Slocum, A. H. (2004). A curved-beam bistable mechanism. *Journal of Microelectromechanical Systems*, 13(2):137–146.

Koh, J.-S. and Cho, K.-J. (2013). Omega-Shaped Inchworm-Inspired Crawling Robot With Large-Index-and-Pitch (LIP) SMA Spring Actuators. *IEEE/ASME Transactions on Mechatronics*, 18(2):419–429. Conference Name: IEEE/ASME Transactions on Mechatronics.

Kohl, M., Krevet, B., and Just, E. (2002). SMA microgripper system. *Sensors and Actuators A: Physical*, 97-98:646–652.

Kyung, J. H., Ko, B. G., Ha, Y. H., and Chung, G. J. (2008). Design of a microgripper for micromanipulation of microcomponents using SMA wires and flexible hinges. *Sensors and Actuators A: Physical*, 141(1):144–150.

Maffiodo, D., Raparelli, T., and Department of Mechanical and Aerospace Engineering, Politecnico di Torino (2017). Three-Fingered Gripper with Flexure Hinges Actuated by Shape Memory Alloy Wires. *International Journal of Automation Technology*, 11(3):355–360.

Must, I., Kaasik, F., Põldsalu, I., Mihkels, L., Johanson, U., Punning, A., and Aabloo, A. (2015). Ionic and Capacitive Artificial Muscle for Biomimetic Soft Robotics. *Advanced Engineering Materials*, 17(1):84–94. _eprint: https://onlinelibrary.wiley.com/doi/pdf/10.1002/adem.201400246.

Rubbert, L., Bitterli, R., Ferrier, N., Fifanski, S., Vardi, I., and Henein, S. (2016). Isotropic springs based on parallel flexure stages. *Precision Engineering*, 43:132–145.

Runciman, A., Xu, D., Pelton, A. R., and Ritchie, R. O. (2011). An equivalent strain/Coffin–Manson approach to multiaxial fatigue and life prediction in superelastic Nitinol medical devices. *Biomaterials*, 32(22):4987–4993.

Shyu, T. C., Damasceno, P. F., Dodd, P. M., Lamoureux, A., Xu, L., Shlian, M., Shtein, M., Glotzer, S. C., and Kotov, N. A. (2015). A kirigami approach to engineering elasticity in nanocomposites through patterned defects. *Nature Materials*, 14(8):785–789.

Sigmund, O. (2011). On the usefulness of non-gradient approaches in topology optimization. *Structural and Multidisciplinary Optimization*, 43(5):589–596.

Talischi, C., Paulino, G. H., Pereira, A., and Menezes, I. F. M. (2012). PolyTop: a Matlab implementation of a general topology optimization framework using unstructured polygonal finite element meshes. *Structural and Multidisciplinary Optimization*, 45(3):329–357.

Tissot-Daguette, L., Smreczak, M., Baur, C., and Henein, S. (2021). Load cell with adjustable stiffness based on a preloaded t-shaped flexure pivot. *euspen's 21st International Conference and Exhibition*.

Tolley, M. T., Shepherd, R. F., Mosadegh, B., Galloway, K. C., Wehner, M., Karpelson, M., Wood, R. J., and Whitesides, G. M. (2014). A Resilient, Untethered Soft Robot. *Soft Robotics*, 1(3):213–223. Publisher: Mary Ann Liebert, Inc., publishers.

Welsch, F., Kirsch, S.-M., Motzki, P., Schmidt, M., and Seelecke, S. (2018). Vacuum Gripper System Based on Bistable SMA Actuation. American Society of Mechanical Engineers Digital Collection.

Zhakypov, Z., Heremans, F., Billard, A., and Paik, J. (2018). An Origami-Inspired Reconfigurable Suction Gripper for Picking Objects With Variable Shape and Size. *IEEE Robotics and Automation Letters*, 3(4):2894–2901.

Zhang, H., Lerner, E., Cheng, B., and Zhao, J. (2020). Compliant Bistable Grippers Enable Passive Perching for Micro Aerial Vehicles. *IEEE/ASME Transactions on Mechatronics*, pages 1–1. Conference Name: IEEE/ASME Transactions on Mechatronics.

Zhang, X. M., Liu, A. Q., Lu, C., and Tang, D. Y. (2007). A Real Pivot Structure for MEMS Tunable Lasers. *Journal of Microelectromechanical Systems*, 16(2):269–278. Conference Name: Journal of Microelectromechanical Systems.

Zhu, B., Zhang, X., Zhang, H., Liang, J., Zang, H., Li, H., and Wang, R. (2020). Design of compliant mechanisms using continuum topology optimization: A review. *Mechanism and Machine Theory*, 143:103622.

Personal details:

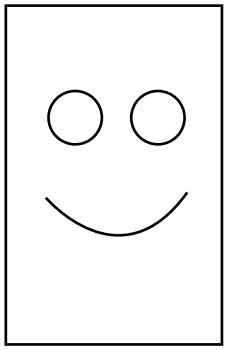

Name :	Mr. Sample CV
Address :	Samplestreet 70 6005 Luzern Switzerland
Date of Birth :	2nd of October 1981
Nationality :	Swiss
Legally work :	legally work in EU
Marital status :	with partner
Children :	none
Languages :	Chinese/Mandarin, English, French, German
Education level :	Bachelors degree
Hospitality work experience :	3-5 years
Special experience :	Europe work experience
Date of availability :	September 2009
Current location :	Africa
Travelling Status :	will be travelling single status
Telephone :	0041 41 370 6759
Email address :	jeff@h-g-r.com
Position(s) sought :	Permanent position for graduates
Department(s) sought :	Food & Beverage Bar/Sommelier

Personal profile:

As a Bachelor of Business Administration and after obtaining first relevant international work experience within the hospitality industry, I am now ready to take on new responsibilities to further my professional career.
My key strengths include strong analytical and logical skills, an eye for detail, communication and interpersonal skills.
I enjoy working in a team and help others progress. At the same time I work well independently.
As a highly motivated and driven individual I strive on taking up challenges.

Interests:

Travelling
Foreign Cultures
Photography
Sports

Educational qualifications:

Oct 99 - Feb 02	Higher Diploma (Hotel Management) Swiss Hotelmanagement School, SHL

Employment history:

Mar 04 - Ongoing	Assistant Manager (Rooms Division/Food & Beverage)
	Hotel Atlantic Kempinski Hamburg www.kempinski.com 5 star business hotel, part of Leading Hotels of the World 412 guest rooms, large function facilities, 3 food & beverage outlets
	Optimization of bar procedures, reinforcing SOPs
	Developing & implementing promotions
	Responsible for day-to-day operations
	Optimization and streamlining of housekeeping and laundry procedures
	Implementation of new SOPs
	Analyzing monthly reports for rooms division performance and sub departments
Mar 03 - Mar 04	Management Trainee
	Hospitality Graduate Recruitment www.h-g-r.com Leading company for placements within the Hospitality industry.
	Traineeship covering all aspects of an online recruitment agency.
Mar 02 - Mar 03	Management Trainee (Rooms Division)
	Hyatt Regency Xian, China www.hyatt.com 5 star business hotel 404 guest rooms, 4 food & beverage outlets
	Traineeship covering all rooms division departments on operational as well as supervisory level.

Training courses attended:

Mar 02 - Ongoing	OpenOffice - IT Courses
May 01 - Jan 03	Language Course - Chinese

References:

Hyatt Regency Xian
Patrick Sawiri, Phone: 86 22 2330 7654

Hospitality Graduate Recruitment
Jeff Ross, Phone: 41 41 370 99 88